Training deep neural density estimators to identify mechanistic models of neural dynamics

Pedro J. Gonçalves[1,2*], **Jan-Matthis Lueckmann**[1,2*], **Michael Deistler**[1*], **Marcel Nonnenmacher**[1,2,3], **Kaan Öcal**[2,4], **Giacomo Bassetto**[1,2], **Chaitanya Chintaluri**[5,6], **William F. Podlaski**[5], **Sara A. Haddad**[7], **Tim P. Vogels**[5,6], **David S. Greenberg**[1,3], **Jakob H. Macke**[1,2,8,9]

***For correspondence:**
pedro.goncalves@caesar.de;
jan-matthis.lueckmann@tum.de;
michael.deistler@tum.de;
Jakob.Macke@uni-tuebingen.de

[*]These authors contributed equally to this work

[1]Computational Neuroengineering, Department of Electrical and Computer Engineering, Technical University of Munich, Germany; [2]Max Planck Research Group Neural Systems Analysis, Center of Advanced European Studies and Research (caesar), Bonn, Germany; [3]Model-Driven Machine Learning, Institute of Coastal Research, Helmholtz Centre Geesthacht; [4]Mathematical Institute, University of Bonn, Bonn, Germany; [5]Centre for Neural Circuits and Behaviour, University of Oxford; [6]Institute of Science and Technology Austria, Klosterneuburg, Austria; [7]Max Planck Institute for Brain Research, Frankfurt, Germany; [8]Machine Learning in Science, Excellence Cluster Machine Learning, Tübingen University, Tübingen, Germany; [9]Max Planck Institute for Intelligent Systems, Tübingen, Germany

---

Abstract Mechanistic modeling in neuroscience aims to explain observed phenomena in terms of underlying causes. However, determining which model parameters agree with complex and stochastic neural data presents a significant challenge. We address this challenge with a machine learning tool which uses deep neural density estimators— trained using model simulations— to carry out Bayesian inference and retrieve the full space of parameters compatible with raw data or selected data features. Our method is scalable in parameters and data features, and can rapidly analyze new data after initial training. We demonstrate the power and flexibility of our approach on receptive fields, ion channels, and Hodgkin–Huxley models. We also characterize the space of circuit configurations giving rise to rhythmic activity in the crustacean stomatogastric ganglion, and use these results to derive hypotheses for underlying compensation mechanisms. Our approach will help close the gap between data-driven and theory-driven models of neural dynamics.

Introduction

New experimental technologies allow us to observe neurons, networks, brain regions and entire systems at unprecedented scale and resolution, but using these data to understand how behavior arises from neural processes remains a challenge. To test our understanding of a phenomenon, we often take to rebuilding it in the form of a computational model that incorporates the mechanisms we believe to be at play, based on scientific knowledge, intuition, and hypotheses about the components of a system and the laws governing their relationships. The goal of such mechanistic models is to investigate whether a proposed mechanism can explain experimental data, uncover details that may have been missed, inspire new experiments, and eventually provide insights into the inner workings of an observed neural or behavioral phenomenon (***Baker et al., 2018***; ***Gerstner et al., 2012***; ***Herz et al., 2006a***; ***O'Leary et al., 2015***). Examples for such a symbiotic relationship between model and experiments range from the now classical work of Hodgkin and Huxley (***Hodgkin and Huxley, 1952***), to population models investigating rules of connectivity, plasticity and network dynamics (***Litwin-Kumar and Doiron, 2012***; ***Potjans and Diesmann, 2012***; ***Prinz et al., 2004***; ***van Vreeswijk and Sompolinsky, 1996***; ***Vogels et al., 2005***), network models of inter-area interactions (***Bassett et al., 2018***; ***Sporns, 2014***), and models of decision making (***Gold and Shadlen, 2007***; ***Wang, 2008***).

A crucial step in building a model is adjusting its free parameters to be consistent with experimental observations. This is essential both for investigating whether the model agrees with reality and for gaining insight into processes which cannot be measured experimentally. For some models in neuroscience, it is possible to identify the relevant parameter regimes from careful mathematical analysis of the model equations. But as the complexity of both neural data and neural models increases, it becomes very difficult to find well-fitting parameters by inspection, and *automated* identification of data-consistent parameters is required.

Furthermore, to understand how a model quantitatively explains data, it is necessary to find not only the *best*, but *all* parameter settings consistent with experimental observations. This is especially important when modeling neural data, where highly variable observations can lead to broad ranges of data-consistent parameters. Moreover, many models in biology are inherently robust to some perturbations of parameters, but highly sensitive to others (***Gutenkunst et al., 2007***; ***O'Leary et al., 2015***), e.g. because of processes such as homeostastic regulation. For these systems, identifying the full range of data-consistent parameters can reveal how multiple distinct parameter settings give rise to the same model behavior (***Achard and De Schutter, 2006***; ***Alonso and Marder, 2019***; ***Foster et al., 1993***; ***Prinz et al., 2004***). Yet, despite the clear benefits of mechanistic models in providing scientific insight, identifying their parameters given data remains a challenging open problem that demands new algorithmic strategies.

The gold standard for automated parameter identification is *statistical inference*, which uses the likelihood $p(\mathbf{x}|\boldsymbol{\theta})$ to quantify the match between parameters $\boldsymbol{\theta}$ and data $\mathbf{x}$. Likelihoods can be efficiently computed for purely statistical models commonly used in neuroscience (***Cunningham and Yu, 2014***; ***Macke et al., 2011***; ***Pandarinath et al., 2018***; ***Pillow et al., 2008***; ***Schneidman et al., 2006***; ***Truccolo et al., 2005***; ***Yu et al., 2009***), but are computationally intractable for most mechanistic models. Mechanistic models are designed to reflect knowledge about biological mechanisms, and not necessarily to be amenable to efficient inference: many mechanistic models are defined implicitly through stochastic computer simulations (e.g. a simulation of a network of spiking neurons), and likelihood calculation would require the ability to integrate over all potential paths through the simulator code. Similarly, a common goal of mechanistic modeling is to capture selected summary features of the data (e.g. a certain firing rate, bursting behavior, etc...), *not* the full dataset in all its details. The same feature (such as a particular average firing rate) can be produced by infinitely many realizations of the simulated process (such as a time-series of membrane potential). This makes it impractical to compute likelihoods, as one would have to average over all possible realizations which produce the same output.

Since the toolkit of (likelihood-based) statistical inference is inaccessible for mechanistic models, parameters are typically tuned ad-hoc (often through laborious, and subjective, trial-and-error), or by computationally expensive parameter search: a large set of models is generated, and grid search (***Prinz et al., 2003***; ***Stringer et al., 2016***; ***Tomm et al., 2011***) or a genetic algorithm (***Druckmann et al., 2007***; ***Hay et al., 2011***; ***Rossant et al., 2011***; ***Van Geit et al., 2016***) is used to filter out simulations which do not match the data. However, these approaches require the user to define a heuristic rejection criterion on which simulations to keep (which can be challenging when observations have many dimensions or multiple units of measurement), and typically end up discarding most simulations. Furthermore, they lack the advantages of statistical inference, which provides

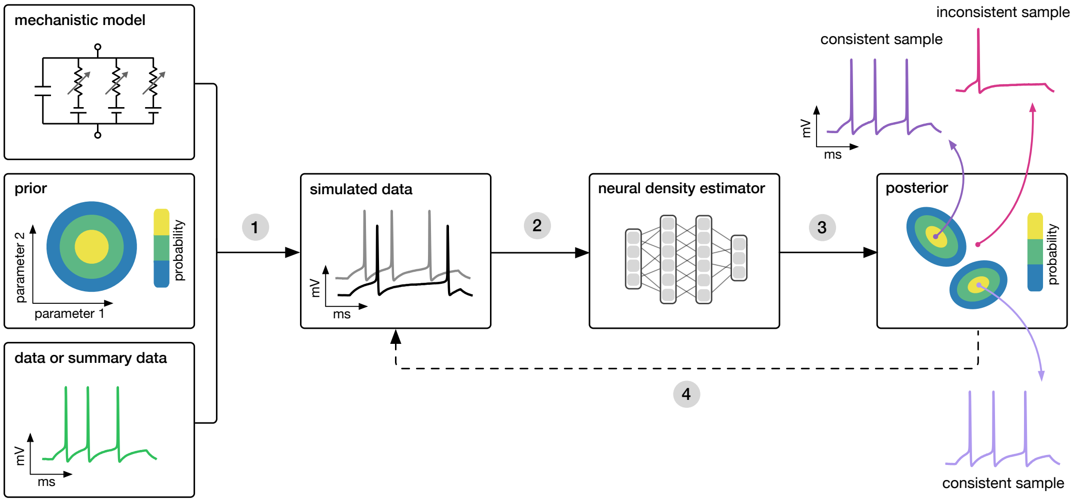

Figure 1. Goal: algorithmically identify mechanistic models which are consistent with data. Our algorithm (SNPE) takes three inputs: a candidate mechanistic model, prior knowledge or constraints on model parameters, and data (or summary statistics). SNPE proceeds by 1) sampling parameters from the prior and simulating synthetic datasets from these parameters, and 2) using a deep density estimation neural network to learn the (probabilistic) association between data (or data features) and underlying parameters, i.e. to learn statistical inference from simulated data. 3) This density estimation network is then applied to empirical data to derive the full space of parameters consistent with the data and the prior, i.e. the posterior distribution. High posterior probability is assigned to parameters which are consistent with both the data and the prior, low probability to inconsistent parameters. 4) If needed, an initial estimate of the posterior can be used to adaptively guide further simulations to produce data-consistent results.

principled approaches for handling variability, quantifying uncertainty, incorporating prior knowledge and integrating multiple data sources. Approximate Bayesian Computation (ABC) (***Beaumont et al., 2002***; ***Marjoram et al., 2003***; ***Sisson et al., 2007***) is a parameter-search technique which aims to perform statistical inference, but still requires definition of a rejection criterion and struggles in high-dimensional problems. Thus, computational neuroscientists face a dilemma: either create carefully designed, highly interpretable mechanistic models (but rely on ad-hoc parameter tuning), or resort to purely statistical models offering sophisticated parameter inference but limited mechanistic insight.

Here we propose a new approach using machine learning to combine the advantages of mechanistic and statistical modeling. We present SNPE (Sequential Neural Posterior Estimation), a tool that makes it possible to perform Bayesian inference on mechanistic models in neuroscience without requiring access to likelihoods. SNPE identifies all mechanistic model parameters consistent with observed experimental data (or summary features). It builds on recent advances in simulation-based Bayesian inference (***Cranmer et al., 2019***; ***Greenberg et al., 2019***; ***Lueckmann et al., 2017***; ***Papamakarios and Murray, 2016***): given observed experimental data (or summary features) $\mathbf{x}_o$, and a mechanistic model with parameters $\boldsymbol{\theta}$, it expresses both prior knowledge and the range of data-compatible parameters through probability distributions. SNPE returns a posterior distribution $p(\boldsymbol{\theta}|\mathbf{x}_o)$ which is high for parameters $\boldsymbol{\theta}$ consistent with both the data $\mathbf{x}_o$ and prior knowledge, but approaches zero for $\boldsymbol{\theta}$ inconsistent with either (Fig. 1).

Similar to parameter search methods, SNPE uses simulations instead of likelihood calculations, but instead of filtering out simulations, it uses *all* simulations to train a multi-layer artificial neural network to identify admissible parameters (Fig. 1). By incorporating modern deep neural networks for conditional density estimation (***Papamakarios et al., 2017***; ***Rezende and Mohamed, 2015***), it can capture the full *distribution* of parameters consistent with the data, even when this distribution has multiple peaks or lies on curved manifolds. Critically, SNPE decouples the design of the model and design of the inference approach, giving the investigator maximal flexibility to design and modify mechanistic models. Our method makes minimal assumptions about the model or its implementation, and can e.g. also be applied to non-differentiable models, such as networks of spiking neurons. Its only requirement is that one can run model simulations for different parameters, and collect the resulting synthetic data or summary features of interest.

While the theoretical foundations of SNPE were originally developed and tested using simple inference problems on small models (***Greenberg et al., 2019***; ***Lueckmann et al., 2017***; ***Papamakarios and Murray, 2016***), here we show that SNPE can scale to complex mechanistic models in neuroscience, provide an accessible and powerful implementation, and develop validation and visualization techniques for exploring the derived posteriors. We illustrate SNPE using mechanistic models expressing key neuroscientific concepts: beginning with a simple neural encoding problem with a known solution, we progress to more complex data types, large datasets and many-parameter models inaccessible to previous methods. We estimate visual receptive fields using many data features, demonstrate rapid inference of ion channel properties from high-throughput voltage-clamp protocols, and show how Hodgkin–Huxley models are more tightly constrained by increasing numbers of data features. Finally, we showcase the power of SNPE by using it to identify the parameters of a network model which can explain an experimentally observed pyloric rhythm in the stomatogastric ganglion (***Prinz et al., 2004***)–in contrast to previous approaches, SNPE allows us to search over the full space of both single-neuron and synaptic parameters, allowing us to study the geometry of the parameter space, as well as to provide new hypotheses for which compensation mechanisms might be at play.

Results

Training neural networks to perform Bayesian inference without likelihood evaluations

SNPE performs Bayesian inference on mechanistic models using only model-simulations, without requiring likelihood evaluations. It requires three inputs: a model (i.e. computer code to simulate data from parameters), prior knowledge or constraints on parameters, and data (outputs from the model or the real system it describes, Fig. 1). SNPE runs simulations for a range of parameter values, and trains an artificial neural network to map any simulation result onto a range of possible parameters. Importantly, a network trained to maximize log-probability (of parameters given simulation results) will learn to approximate the posterior distribution as given by Bayes rule (***Papamakarios and Murray, 2016***) (see Methods for details, Fig. 1). After training on *simulated* data with known model parameters, SNPE can perform Bayesian inference of unknown parameters for *empirical* data. This approach to Bayesian inference never requires evaluating likelihoods. SNPE's efficiency can be further improved by using the running estimate of the posterior distribution to guide further simulations towards data-compatible regions of the parameter space (***Greenberg et al., 2019***; ***Lueckmann et al., 2017***; ***Papamakarios and Murray, 2016***). Below, we apply SNPE to a range of stochastic models in neuroscience.

Estimating stimulus-selectivity in linear-nonlinear encoding models

We first illustrate SNPE on linear-nonlinear (LN) encoding models, a special case of generalized linear models (GLMs). These are simple, commonly used phenomenological models for which likelihood-based parameter estimation is feasible (***Brown et al., 1998***; ***Gerwinn et al., 2010***; ***Paninski, 2004***; ***Pillow, 2007***; ***Pillow and Scott, 2012***; ***Polson et al., 2013***), and which can be used to validate the accuracy of our approach, before applying SNPE to more complex models for which the likelihood is unavailable. We will show that SNPE returns the correct posterior distribution over parameters, that it can cope with high-dimensional observation data, that it can recover multiple solutions to parameter inference problems, and that it is substantially more simulation efficient than conventional rejection-based ABC methods.

An LN model describes how a neuron's firing rate is modulated by a sensory stimulus through a

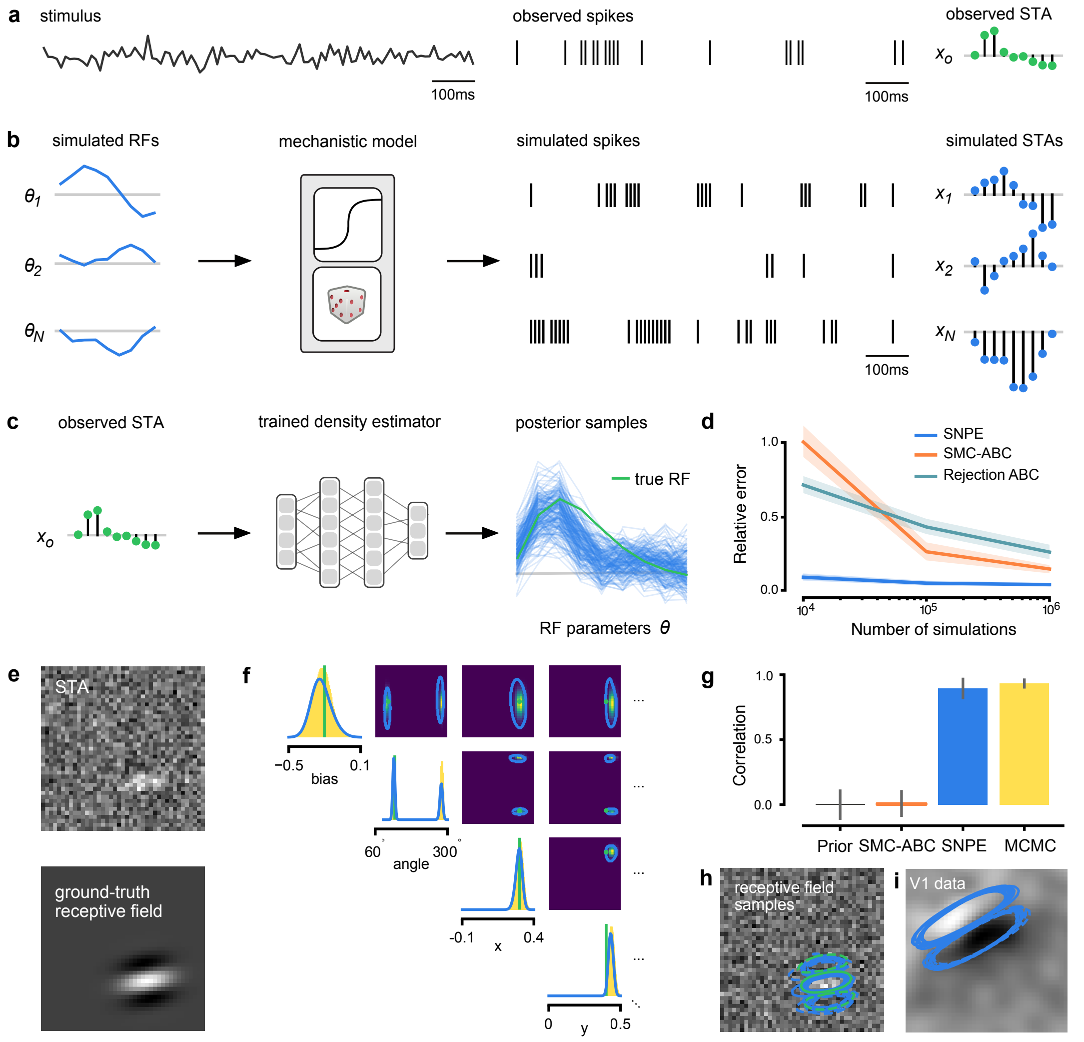

Figure 2. Estimating receptive fields in linear-nonlinear models of single neurons with statistical inference (a) Schematic of a time-varying stimulus, associated observed spike train and resulting spike-triggered average (STA) (b) SNPE proceeds by first randomly generating simulated receptive fields θ, and using the mechanistic model (here an LN model) to generate simulated spike trains and simulated STAs. (c) These simulated STAs and receptive fields are then used to train a deep neural density estimator to identify the distribution of receptive fields consistent with a given observed STA $\mathbf{x}_o$. (d) Relative error in posterior estimation between SNPE and alternative methods (mean and 95%CI; 0 corresponds to perfect estimation, 1 to prior-level, details in Methods). (e) Example of spatial receptive field. We simulated responses and an STA of a LN-model with oriented receptive field. (f) We used SNPE to recover the distribution of receptive-field parameters. Univariate and pairwise marginals for four parameters of the spatial filter (MCMC, yellow histograms; SNPE, blue lines; ground truth, green ; full posterior in Supplementary Fig. 4). Non-identifiabilities of the Gabor parameterization lead to multimodal posteriors. (g) Average correlation (±SD) between ground-truth receptive field and receptive field samples from posteriors inferred with SMC-ABC, SNPE, and MCMC (which provides an upper bound given the inherent stochasticity of the data). (h) Posterior samples from SNPE posterior (SNPE, blue) compared to ground-truth receptive field (green; see panel (e)), overlaid on STA. (i) Posterior samples for V1 data; full posterior in Supplementary Fig. 6.

---

linear filter $\boldsymbol{\theta}$, often referred to as the *receptive field* (***Chichilnisky, 2001***; ***Pillow et al., 2005***). We first considered a model of a retinal ganglion cell (RGC) driven by full-field flicker (Fig. 2a). A statistic that is often used to characterize such a neuron is the *spike-triggered average* (STA) (Fig. 2a, right). We therefore used the STA, as well as the firing rate of the neuron, as input $\mathbf{x}_o$ to SNPE. (Note that, in the limit of infinite data, and for white noise stimuli, the STA will converge to the receptive field (***Paninski, 2004***)–for finite, and non-white data, the two will in general be different.) Starting with random receptive fields θ, we generated synthetic spike trains and calculated STAs from them (Fig. 2b). We then trained a neural conditional density estimator to recover the receptive fields from the STAs and firing rates (Fig. 2c). This allowed us to estimate the posterior distribution over receptive fields, i.e. to estimate which receptive fields are consistent with the data (and prior) (Fig. 2c). For LN models, likelihood-based inference is possible, allowing us to validate the SNPE posterior by comparing it to a reference posterior obtained via Markov Chain Monte Carlo (MCMC) sampling (***Pillow and Scott, 2012***; ***Polson et al., 2013***). We found that SNPE accurately estimates the posterior distribution (Supplementary Fig. 1 and Supplementary Fig. 2), and substantially outperforms Sequential Monte Carlo (SMC) ABC methods (***Beaumont et al., 2009***; ***Sisson et al., 2007***) (Fig. 2d). If SNPE works correctly, its posterior mean filter will match that of the reference posterior– however, it is not to be expected that either of them precisely matches the ground-truth filter (Fig. 2c and Supplementary Fig. 1): In the presence of finite sampling and stochasticity, multiple different filters could have plausibly given rise to the observed data. A properly inferred posterior will reflect this uncertainty, and include the true filters as one of many plausible explanations of the data (but not necessarily as the 'mean' of all plausible explanations) (Supplementary Fig. 2). Increasing the number of Bernoulli samples in the observed data leads to progressively tighter posteriors, with posterior samples closer to the true filter (Supplementary Fig. 3). Furthermore, SNPE closely agrees with the MCMC reference solution in all these cases, further emphasizing the correctness of the posteriors inferred with SNPE.

As a more challenging problem, we inferred the receptive field of a neuron in primary visual cortex (V1) (***Dyballa et al., 2018***; ***Niell and Stryker, 2008***). Using a model composed of a bias (related to the spontaneous firing rate) and a Gabor function with 8 parameters (***Jones and Palmer, 1987***) describing the receptive field's location, shape and strength, we simulated responses to 5-minute random noise movies of 41×41 pixels, such that the STA is high-dimensional, with a total of 1681 dimensions (Fig. 2e). This problem admits multiple solutions (as e.g. rotating the receptive field by 180°). As a result, the posterior distribution has multiple peaks ('modes'). Starting from a simulation result $\mathbf{x}_o$ with known parameters, we used SNPE to estimate the posterior distribution $p(\boldsymbol{\theta}|\mathbf{x}_o)$. To deal with the high-dimensional data $\mathbf{x}_o$ in this problem, we used a convolutional neural network (CNN), as this architecture excels at learning relevant features from image data (***Krizhevsky et al., 2012***; ***Simonyan and Zisserman, 2015***). To deal with the multiple peaks in the posterior, we fed the CNN's output into a mixture density network (MDN) (***Bishop, 1994***), which can learn to assign probability distributions with multiple peaks as a function of its inputs (details in Methods). Using this strategy, SNPE was able to infer a posterior distribution that tightly enclosed the ground truth simulation parameters which generated the original simulated data $\mathbf{x}_o$, and matched a reference MCMC posterior (Fig. 2f, posterior over all parameters in Supplementary Fig. 4). For this challenging estimation problem with high-dimensional summary features, an SMC-ABC algorithm with the same simulation-budget failed to identify the correct receptive fields (Fig. 2g) and posterior distributions (Supplementary Fig. 5). We also applied this approach to electrophysiological data from a V1 cell (***Dyballa et al., 2018***), identifying a sine-shaped Gabor receptive field consistent with the original spike-triggered average (Fig. 2i; posterior distribution in Supplementary Fig. 6).

Functional diversity of ion channels: efficient high-throughput inference

We next show how SNPE can be efficiently applied to estimation problems in which we want to identify a large number of models for different observations in a database. We considered a flexible model of ion channels (***Destexhe and Huguenard, 2000***), which we here refer to as the *Omnimodel*. This model uses 8 parameters to describe how the dynamics of currents through non-inactivating potassium channels depend on membrane voltage (Fig. 3a). For various choices of its parameters θ, it can capture 350 specific models in publications describing this channel type, cataloged in the IonChannelGenealogy (ICG) database (***Podlaski et al., 2017***). We aimed to identify these ion channel parameters $\boldsymbol{\theta}$ for each ICG model, based on 11 features of the model's response to a sequence of 5 noisy voltage clamp protocols, resulting in a total of 55 different characteristic features per model

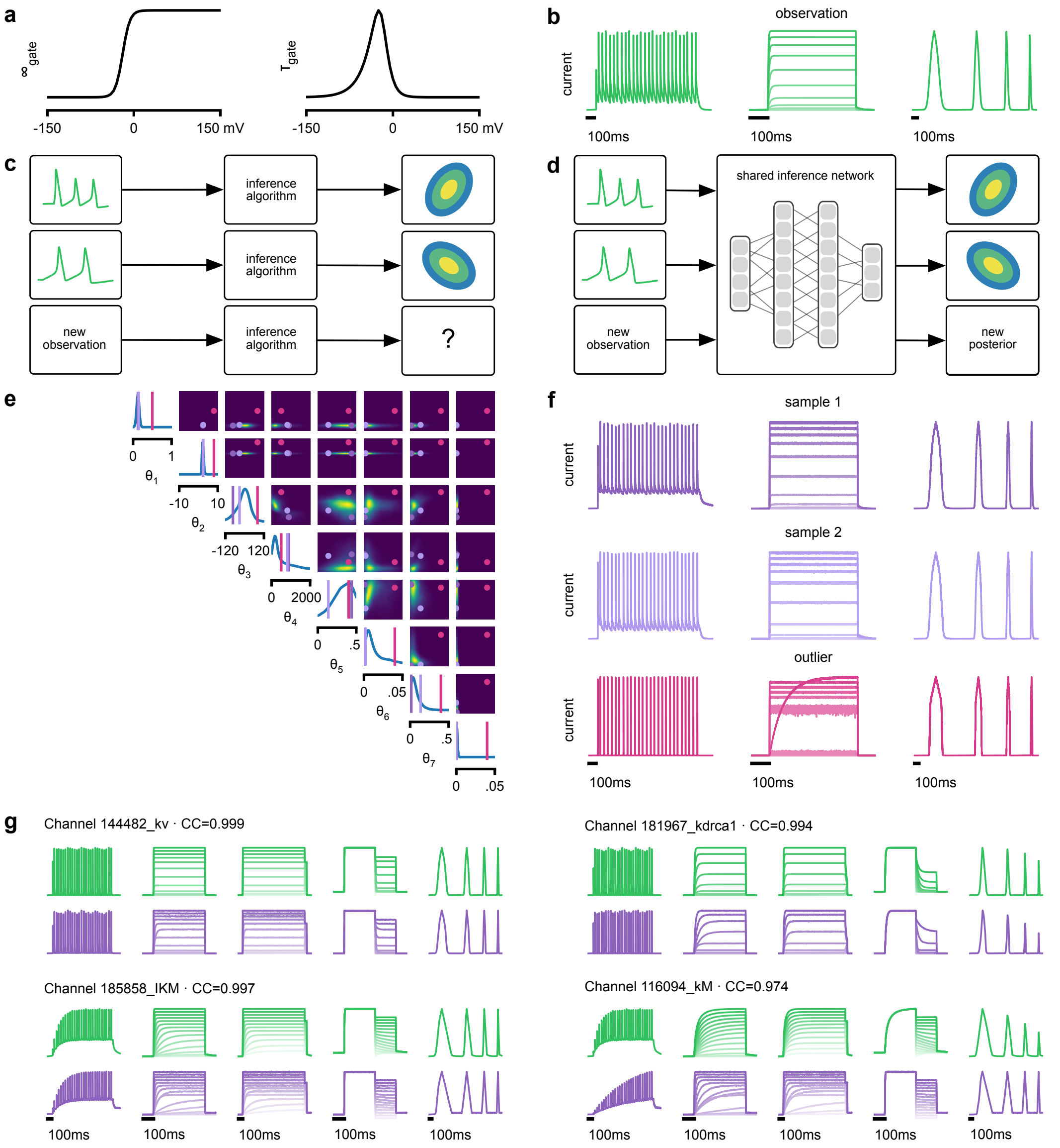

Figure 3. Inference on a database of ion-channel models. (a) We perform inference over the parameters of non-inactivating potassium channel models. Channel kinetics are described by steady-state activation curves, ∞_{gate}, and time-constant curves, τ_{gate}. (b) Observation generated from a channel model from ICG database: normalized current responses to three (out of five) voltage-clamp protocols (action potentials, activation, and ramping). Details in ***Podlaski et al.*** (***2017***). (c) Classical approach to parameter identification: inference is optimized on each datum separately, requiring new computations for each new datum. (d) Amortized inference: an inference network is learned which can be applied to multiple data, enabling rapid inference on new data. (e) Posterior distribution over eight model parameters, θ_1 to θ_8. Ground truth parameters in green, high-probability parameters in purple, low-probability parameters in magenta. (f) Traces obtained by sampling from the posterior in (e). Purple: traces sampled from posterior, i.e. with high posterior probability. Magenta: trace from parameters with low probability. (g) Observations (green) and traces generated by posterior samples (purple) for four models from the database.

(Fig. 3b, see Methods for details).

Because this model's output is a typical format for functional characterization of ion channels both in simulations (***Podlaski et al., 2017***) and in high-throughput electrophysiological experiments (***Dunlop et al., 2008***; ***Ranjan et al., 2019***; ***Suk et al., 2019***), the ability to rapidly infer different parameters for many separate experiments is advantageous. Existing fitting approaches based on numerical optimization (***Destexhe and Huguenard, 2000***; ***Ranjan et al., 2019***) must repeat all computations anew for a new experiment or data point (Fig. 3c). However, for SNPE the only heavy computational tasks are carrying out simulations to generate training data, and training the neural network. We therefore reasoned that by training a network once using a large number of simulations, we could subsequently carry out rapid 'amortized' parameter inference on new data using a single pass through the network (Fig. 3d) (***Speiser et al., 2017***; ***Webb et al., 2018***). To test this idea, we used SNPE to train a neural network to infer the posterior from any data $\mathbf{x}$. To generate training data, we carried out 1 million Omnimodel simulations, with parameters randomly chosen across ranges large enough to capture the models in the ICG database (***Podlaski et al., 2017***). SNPE was run using a single round, i.e. it learned to perform inference for all data from the prior (rather than a specific observed datum). Generating these simulations took around 1000 CPU-hours and training the network 150 CPU-hours, but afterwards a full posterior distribution could be inferred for new data in less than 10 ms.

As a first test, SNPE was run on simulation data, generated by a previously published model of a non-inactivating potassium channel (***McTavish et al., 2012***) (Fig. 3b). Simulations of the Omnimodel using parameter sets sampled from the obtained posterior distribution (Fig. 3e) closely resembled the input data on which the SNPE-based inference had been carried out, while simulations using 'outlier' parameter sets with low probability under the posterior generated current responses that were markedly different from the data $\mathbf{x}_o$ (Fig. 3f). Taking advantage of SNPE's capability for rapid amortized inference, we further evaluated its performance on all 350 non-inactivating potassium channel models in ICG. In each case, we carried out a simulation to generate initial data from the original ICG model, used SNPE to calculate the posterior given the Omnimodel, and then generated a new simulation $\mathbf{x}$ using parameters sampled from the posterior (Fig. 3f). This resulted in high correlation between the original ICG model response and the Omnimodel response, in every case (>0.98 for more than 90% of models, see Supplementary Fig. 7). However, this approach was not able to capture all traces perfectly, as e.g. it failed to capture the shape of the onset of the bottom right model in Fig. 3g. Additional analysis of this example revealed that this example is not a failure of SNPE, but rather a limitation of the Omnimodel: in particular, directly fitting the steady-state activation and time-constant curves on this specific example yielded no further quantitative or qualitative improvement, suggesting that the limitation is in the model, not the fit. Thus, SNPE can be used to reveal limitations of candidate models and aid the development of more verisimilar mechanistic models.

Calculating the posterior for all 350 ICG models took only a few seconds, and was fully automated, i.e. did not require user interactions. These results show how SNPE allows fast and accurate identification of biophysical model parameters on new data, and how SNPE can be deployed for applications requiring rapid automated inference, such as high-throughput screening-assays, closed-loop paradigms (e.g. for adaptive experimental manipulations or stimulus-selection (***Kleinegesse and Gutmann, 2019***)), or interactive software tools.

Hodgkin–Huxley model: stronger constraints from additional data features

The Hodgkin–Huxley (HH) model (***Hodgkin and Huxley, 1952***) of action potential generation through ion channel dynamics is a highly influential mechanistic model in neuroscience. A number of algorithms have been proposed for fitting HH models to electrophysiological data (***Ben-Shalom et al., 2019***; ***Huys et al., 2006***; ***Meliza et al., 2014***; ***Pospischil et al., 2008***; ***Prinz et al., 2003***; ***Rossant et al., 2011***; ***Van Geit et al., 2016***), but (with the exception of ***Daly et al., 2015***) these approaches do not attempt to estimate the full posterior. Given the central importance of the HH model in neuroscience, we sought to test how SNPE would cope with this challenging non-linear model.

As previous approaches for HH models concentrated on reproducing specified features (e.g. the number of spikes, ***Pospischil et al., 2008***), we also sought to determine how various features provide different constraints. We considered the problem of inferring 8 biophysical parameters in a HH single-compartment model, describing voltage-dependent sodium and potassium conductances and other intrinsic membrane properties, including neural noise, making the model stochastic by

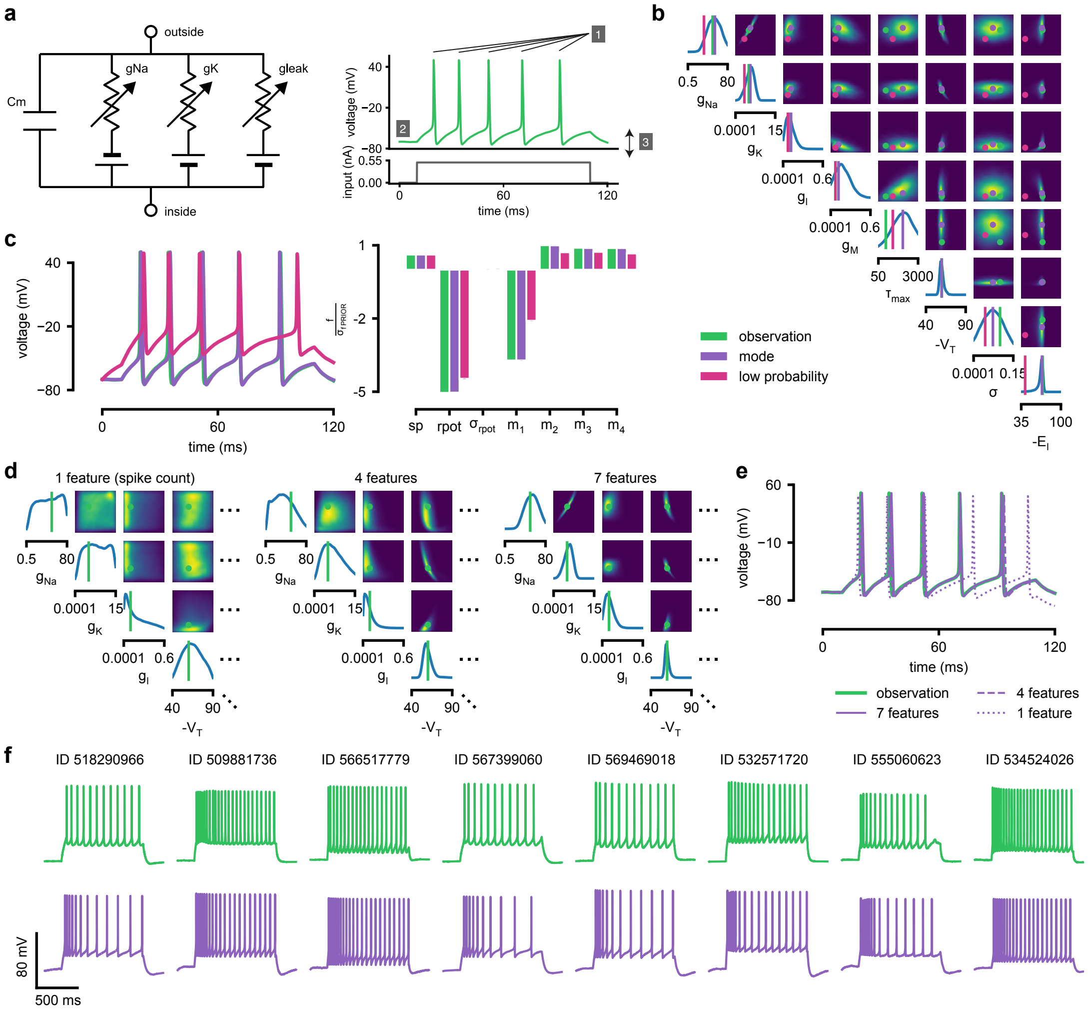

Figure 4. Inference for single compartment Hodgkin–Huxley model. (a) Circuit diagram describing the Hodgkin–Huxley model (left), and simulated voltage-trace given a current input (right). 3 out of 7 voltage features are depicted: (1) number of spikes, (2) mean resting potential and (3) standard deviation of the pre-stimulus resting potential. (b) Inferred posterior for 8 parameters given 7 voltage features. Ground truth parameters in green, high-probability parameters in purple, low-probability parameters in magenta. (c) Traces (left) and associated features f (right) for the desired output (observation), the mode of the inferred posterior, and a sample with low posterior probability. The voltage features are: number of spikes sp, mean resting potential $rpot$, standard deviation of the resting potential σ_{rpot}, and the first 4 voltage moments, mean m_1, standard deviation m_2, skewness m_3 and kurtosis m_4. Each value plotted is the mean feature ± standard deviation across 100 simulations with the same parameter set. Each feature is normalized by $\sigma_{\text{f PRIOR}}$, the standard deviation of the respective feature of simulations sampled from the prior. (d) Partial view of the inferred posteriors (4 out of 8 parameters) given 1, 4 and 7 features (full posteriors over 8 parameters in Supplementary Fig. 8). (e) Traces for posterior modes given 1, 4 and 7 features. Increasing the number of features leads to posterior traces that are closer to the observed data. (f) Observations from Allen Cell Types Database (green) and corresponding mode samples (purple). Posteriors in Supplementary Fig. 9.

nature (Fig. 4a, left). We simulated the neuron's voltage response to the injection of a square wave of depolarizing current, and defined the model output $\mathbf{x}$ used for inference as the number of evoked action potentials along with 6 additional features of the voltage response (Fig. 4a, right, details in Methods). We first applied SNPE to observed data $\mathbf{x}_o$ created by simulation from the model, calculating the posterior distribution using all 7 features in the observed data (Fig. 4b). The posterior contained the ground truth parameters in a high probability-region, as in previous applications, indicating the consistency of parameter identification. The variance of the posterior was narrower for some parameters than for others, indicating that the 7 data features constrain some parameters strongly (such as the potassium conductance), but others only weakly (such as the adaptation time constant). Additional simulations with parameters sampled from the posterior closely resembled the observed data $\mathbf{x}_o$, in terms of both the raw membrane voltage over time and the 7 data features (Fig. 4c, purple and green). Parameters with low posterior probability (outliers) generated simulations that markedly differed from $\mathbf{x}_o$ (Fig. 4c, magenta).

Genetic algorithms are commonly used to fit parameters of deterministic biophysical models (***Druckmann et al., 2007***; ***Gouwens et al., 2018***; ***Hay et al., 2011***; ***Van Geit et al., 2016***). While genetic algorithms can also return multiple data-compatible parameters, they do not perform inference (i.e. find the posterior distribution), and their outputs depend strongly on user-defined goodness-of-fit criteria. When comparing a state-of-the-art genetic algorithm (Indicator Based Evolutionary Algorithm, IBEA, ***Bleuler et al., 2003***; ***Van Geit et al., 2016***; ***Zitzler and Künzli, 2004***) to SNPE, we found that the parameter-settings favoured by IBEA produced simulations whose summary features were as similar to the observed data as those obtained by SNPE high-probability samples (Supplementary Fig. 10). However, high-scoring IBEA parameters were concentrated in small regions of the posterior, i.e. IBEA did not identify the full space of data-compatible models.

To investigate how individual data features constrain parameters, we compared SNPE-estimated posteriors based 1) solely on the spike count, 2) on the spike count and 3 voltage-features, or 3) on all 7 features of $\mathbf{x}_o$. As more features were taken into account, the posterior became narrower and centered more closely on the ground truth parameters (Fig. 4d, Supplementary Fig. 8). Posterior simulations matched the observed data only in those features that had been used for inference (e.g. applying SNPE to spike counts alone identified parameters that generated the correct number of spikes, but for which spike timing and subthreshold voltage time course were off, Fig. 4e). For some parameters, such as the potassium conductance, providing more data features brought the peak of the posterior (the *posterior mode*) closer to the ground truth and also decreased uncertainty. For other parameters, such as V_T, a parameter adjusting the spike threshold (***Pospischil et al., 2008***), the peak of the posterior was already close to the correct value with spike counts alone, but adding additional features reduced uncertainty. While SNPE can be used to study the effect of additional data features in reducing parameter uncertainty, this would not be the case for methods that only return a single best-guess estimate of parameters. These results show that SNPE can reveal how information from multiple data features imposes collective constraints on channel and membrane properties in the HH model.

We also inferred HH parameters for 8 *in vitro* recordings from the Allen Cell Types database using the same current-clamp stimulation protocol as in our model (***Allen Institute for Brain Science, 2016***; ***Teeter et al., 2018***) (Fig. 4f, Supplementary Fig. 9). In each case, simulations based on the SNPE-inferred posterior closely resembled the original data (Fig. 4f). We note that while inferred parameters differed across recordings, some parameters (the spike threshold, the density of sodium channels, the membrane reversal potential and the density of potassium channels) were consistently more strongly constrained than others (the intrinsic neural noise, the adaptation time constant, the density of slow voltage-dependent channels and the leak conductance) (Supplementary Fig. 9). Overall, these results suggest that the electrophysiological responses measured by this current-clamp protocol can be approximated by a single-compartment HH model, and that SNPE can identify the admissible parameters.

Crustacean stomatogastric ganglion: sensitivity to perturbations

We next aimed to demonstrate how the full posterior distribution obtained with SNPE can lead to novel scientific insights. To do so, we used the pyloric network of the stomatogastric ganglion (STG) of the crab *Cancer borealis*, a well-characterized neural circuit producing rhythmic activity. In this circuit, similar network activity can arise from vastly different sets of membrane and synaptic conductances (***Prinz et al., 2004***). We first investigated whether data-consistent sets of membrane and synaptic conductances are connected in parameter space, as has been demonstrated for sin-

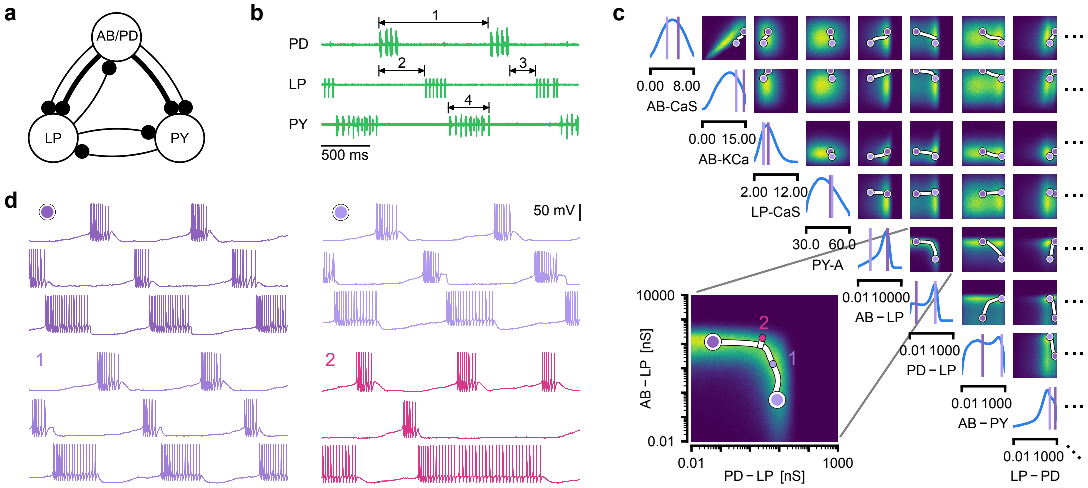

Figure 5. Identifying network models underlying an experimentally observed pyloric rhythm in the crustacean stomatogastric ganglion. (a) Simplified circuit diagram of the pyloric network from the stomatogastric ganglion. Thin connections are fast glutamatergic, thick connections are slow cholinergic. (b) Extracellular recordings from nerves of pyloric motor neurons of the crab *Cancer borealis* (***Haddad and Marder, 2018***). Numbers indicate some of the used summary features, namely cycle period (1), phase delays (2), phase gaps (3), and burst durations (4) (see Methods for details). (c) Posterior over 24 membrane and 7 synaptic conductances given the experimental observation shown in panel b (8 parameters shown, full posterior in Supplementary Fig. 11). Two high-probability parameter sets in purple. Inset: magnified marginal posterior for the synaptic strengths AB to LP neuron vs. PD to LP neuron. (d) Identifying directions of sloppiness and stiffness. Two samples from the posterior both show similar network activity as the experimental observation (top left and top right), but have very different parameters (purple dots in panel c). Along the high-probability path between these samples, network activity is preserved (trace 1). When perturbing the parameters orthogonally off the path, network activity changes abruptly and becomes non-pyloric (trace 2).

---

gle neurons (***Taylor et al., 2006***), and, second, which compensation mechanisms between parameters of this circuit allow the neural system to maintain its activity despite parameter variations. While this model has been studied extensively, answering these questions requires characterizing higher-dimensional parameter spaces than those accessed previously. We demonstrate how SNPE can be used to identify the posterior distribution over both membrane and synaptic conductances of the STG (31 parameters total) and how the full posterior distribution can be used to study the above questions at the circuit level.

For some biological systems, multiple parameter sets give rise to the same system behavior (***Alonso and Marder, 2019***; ***Fisher et al., 2013***; ***Gutierrez et al., 2013***; ***Marder and Goaillard, 2006***; ***Marder et al., 2015***; ***Prinz et al., 2004***). In particular, neural systems can be robust to specific perturbations of parameters (***Marder et al., 2015***; ***O'Leary and Marder, 2016***; ***O'Leary et al., 2014***), yet highly sensitive to others, properties referred to as *sloppiness* and *stiffness* (***Goldman et al., 2001***; ***Gutenkunst et al., 2007***; ***Machta et al., 2013***; ***O'Leary et al., 2015***). We studied how perturbations affect model output using a model (***Prinz et al., 2004***) and data (***Haddad and Marder, 2018***) of the pyloric rhythm in the crustacean stomatogastric ganglion (STG). This model describes a triphasic motor pattern generated by a well-characterized circuit (Fig. 5a). The circuit consists of two electrically coupled pacemaker neurons (anterior burster and pyloric dilator, AB/PD), modeled as a single neuron, as well as two types of follower neurons (lateral pyloric (LP) and pyloric (PY)), all connected through inhibitory synapses (details in Methods). Eight membrane conductances are included for each modeled neuron, along with 7 synaptic conductances, for a total of 31 parameters. This model has been used to demonstrate that virtually indistinguishable activity can arise from vastly different membrane and synaptic conductances in the STG (***Alonso and Marder, 2019***; ***Prinz et al., 2004***). Here, we build on these studies and extend the model to include intrinsic neural noise on each neuron (see Methods).

We applied SNPE to an extracellular recording from the STG of the crab *Cancer borealis* (***Haddad and Marder, 2018***) which exhibited pyloric activity (Fig. 5b), and inferred the posterior distribution over all 31 parameters based on 18 salient features of the voltage traces, including cycle period, phase delays, phase gaps, and burst durations (features in Fig. 5B, posterior in Fig. 5c, posterior over all parameters in Supplementary Fig. 11, details in Methods). Consistent with previous reports, the posterior distribution has high probability over extended value ranges for many membrane and synaptic conductances. To verify that parameter settings across these extended ranges are indeed capable of generating the experimentally observed network activity, we sampled two sets of membrane and synaptic conductances from the posterior distribution. These two samples have widely disparate parameters from each other (Fig. 5c, purple dots, details in Methods), but both exhibit activity highly similar to the experimental observation (Fig. 5d, top left and top right).

We then investigated the geometry of the parameter space producing these rhythms (***Achard and De Schutter, 2006***; ***Alonso and Marder, 2019***). First, we wanted to identify directions of sloppiness, and we were interested in whether parameter settings producing pyloric rhythms form a single connected region, as has been shown for single neurons (***Taylor et al., 2006***), or whether they lie on separate 'islands'. Starting from the two above parameter settings showing similar activity, we examined whether they were connected by searching for a path through parameter space along which pyloric activity was maintained. To do this, we algorithmically identified a path lying only in regions of high posterior probability (Fig. 5c, white, details in Methods). Along the path, network output was tightly preserved, despite a substantial variation of the parameters (voltage trace 1 in Fig. 5d, Supplementary Fig. 12a,c). Second, we inspected directions of stiffness by perturbing parameters off the path. We applied perturbations that yield maximal drops in posterior probability (see Methods for details), and found that the network quickly produced non-pyloric activity (voltage trace 2, Fig. 5d) (***Goldman et al., 2001***). Note that, while parameter set 2 seems to lie in regions of high probability when inspecting pairwise marginals, it in fact has low probability under the full posterior distribution (Supplementary Fig. 13). In identifying these paths and perturbations, we exploited the fact that SNPE provides a differentiable estimate of the posterior, as opposed to parameter search methods which provide only discrete samples.

Overall, these results show that the pyloric network can be robust to specific perturbations in parameter space, but sensitive to others, and that one can interpolate between disparate solutions while preserving network activity. This analysis demonstrates the flexibility of SNPE in capturing complex posterior distributions, and shows how the differentiable posterior can be used to study directions of sloppiness and stiffness.

Predicting compensation mechanisms from posterior distributions

Experimental and computational studies have shown that stable neural activity can be maintained despite variable circuit parameters (***Marder and Taylor, 2011***; ***O'Leary, 2018***; ***Prinz et al., 2004***). This behavior can emerge from two sources (***Marder and Taylor, 2011***): either, the variation of a certain parameter barely influences network activity at all, or alternatively, variations of several parameters influence network activity, but their effects compensate for one another. Here, we investigated these possibilities by using the posterior distribution over membrane and synaptic conductances of the STG.

We began by drawing samples from the posterior and inspecting their pairwise histograms (i.e. the pairwise marginals, Fig. 6a, posterior over all parameters in Supplementary Fig. 11). Consistent with previously reported results (***Taylor et al., 2009***), many parameters seem only weakly constrained and only weakly correlated (Fig. 6b). However, this observation does not imply that the parameters of the network do not have to be finely tuned: pairwise marginals are averages over many network configurations, where all other parameters may take on diverse values, which could disguise that each individual configuration is finely tuned. Indeed, when we sampled parameters independently from their posterior histograms, the resulting circuit configurations rarely produced

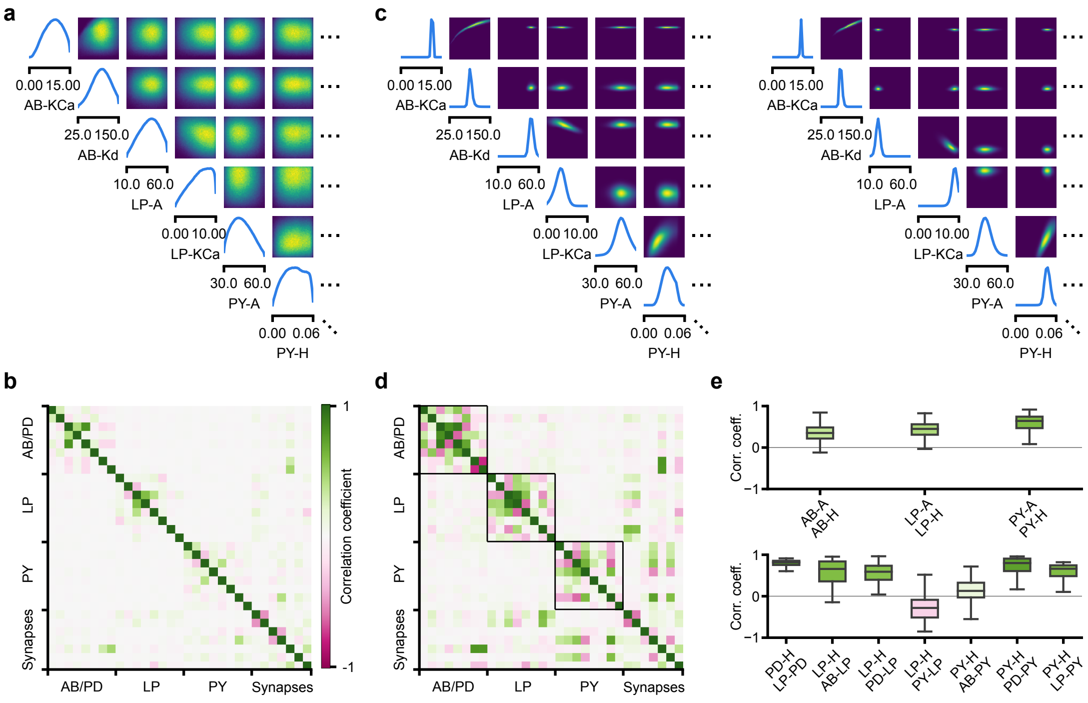

Figure 6. Predicting compensation mechanisms in the stomatogastric ganglion. (a) Inferred posterior. We show a subset of parameters which are weakly constrained (full posterior in Supplementary Fig. 11). Pyloric activity can emerge from a wide range of maximal membrane conductances, as the 1D and 2D posterior marginals cover almost the entire extent of the prior. (b) Correlation matrix, based on the samples shown in panel a. Almost all correlations are weak. Ordering of membrane and synaptic conductances as in Supplementary Fig. 11. (c) Conditional distributions given a particular circuit configuration: for the plots on the diagonal, we keep all but one parameter fixed. For plots above the diagonal, we keep all but two parameters fixed. The remaining parameter(s) are narrowly tuned; tuning across parameters is often highly correlated. When conditioning on a different parameter setting (right plot), the conditional posteriors change, but correlations are often maintained. (d) Conditional correlation matrix, averaged over 500 conditional distributions like the ones shown in panel c. Black squares highlight parameter-pairs within the same model neuron. (e) Consistency with experimental observations. Top: maximal conductance of the fast transient potassium current and the maximal conductance of the hyperpolarization current are positively correlated for all three neurons. This has also been experimentally observed in the PD and the LP neuron (***MacLean et al., 2005***). Bottom: the maximal conductance of the hyperpolarization current of the postsynaptic neuron can compensate the strength of the synaptic input, as experimentally observed in the PD and the LP neuron (***Grashow et al., 2010***; ***Marder, 2011***). The boxplots indicate the maximum, 75% quantile, median, 25% quantile, and minimum across 500 conditional correlations for different parameter pairs. Face color indicates mean correlation using the colorbar shown in panel b.

---

pyloric activity, indicating that parameters have to be tuned relative to each other (Supplementary Fig. 14). This analysis also illustrates that the (common) approach of independently setting parameters can be problematic: although each parameter individually is in a realistic range, the network as a whole is not (***Golowasch et al., 2002***). Finally, it shows the importance of identifying the full posterior distribution, which is far more informative than just finding individual parameters and assigning error bars.

In order to investigate the need for tuning between pairs of parameters, we held all but two parameters constant at a given consistent circuit configuration (sampled from the posterior), and observed the network activity across different values of the remaining pair of parameters. We can do so by calculating the conditional posterior distribution (details in Methods), and do not have to generate additional simulations (as would be required by parameter search methods). Doing so has a simple interpretation: when all but two parameters are fixed, what values of the remaining two parameters can then lead to the desired network activity? We found that the desired pattern of pyloric activity can emerge only from narrowly tuned and often highly correlated combinations of the remaining two parameters, showing how these parameters can compensate for one another (Fig. 6c). When repeating this analysis across multiple network configurations, we found that these 'conditional correlations' are often preserved (Fig. 6c, left and right). This demonstrates that pairs of parameters can compensate for each other in a similar way, independently of the values taken by other parameters. This observation about compensation could be interpreted as an instance of modularity, a widespread underlying principle of biological robustness (***Kitano, 2004***).

We calculated conditional correlations for each parameter pair using 500 different circuit configurations sampled from the posterior (Fig. 6d). Compared to correlations based on the pairwise marginals (Fig. 6b), these conditional correlations were substantially stronger. They were particularly strong across membrane conductances of the same neuron, but primarily weak across different neurons (black boxes in Fig. 6d).

Finally, we tested whether the conditional correlations were in line with experimental observations. For the PD and the LP neuron, it has been reported that overexpression of the fast transient potassium current (I_A) leads to a compensating increase of the hyperpolarization current (I_H), suggesting a positive correlation between these two currents (***MacLean et al., 2005***, ***2003***). These results are qualitatively consistent with the positive conditional correlations between the maximal conductances of I_A and I_H for all three model neurons (Fig. 6e top). In addition, using the dynamic clamp, it has been shown that diverse combinations of the synaptic input strength and the maximal conductance of I_H lead to similar activity in the LP and the PD neuron (***Grashow et al., 2010***; ***Marder, 2011***). Consistent with these findings, the non-zero conditional correlations reveal that there can indeed be compensation mechanisms between the synaptic strength and the maximal conductance of I_H of the postsynaptic neuron (Fig. 6e bottom).

Overall, we showed how SNPE can be used to study parameter dependencies, and how the posterior distribution can be used to efficiently explore potential compensation mechanisms. We found that our method can predict compensation mechanisms which are qualitatively consistent with experimental studies. We emphasize that these findings would not have been possible with a direct grid-search over all parameters: defining a grid in a 31-dimensional parameter space would require more than $2^{31} >$2 billion simulations, even if one were to use the coarsest-possible grid with only 2 values per dimension.

Discussion

How can we build models which give insights into the causal mechanisms underlying neural or behavioral dynamics? The cycle of building mechanistic models, generating predictions, comparing them to empirical data, and rejecting or refining models has been of crucial importance in the empirical sciences. However, a key challenge has been the difficulty of identifying mechanistic models which can quantitatively capture observed phenomena. We suggest that a generally applicable tool to constrain mechanistic models by data would expedite progress in neuroscience. While many considerations should go into designing a model that is appropriate for a given question and level of description (***Brette, 2015***; ***Gerstner et al., 2012***; ***Herz et al., 2006b***; ***O'Leary et al., 2015***), the question of whether and how one can perform statistical inference should not compromise model design. In our tool, SNPE, the process of model building and parameter inference are entirely decoupled. SNPE can be applied to *any* simulation-based model (requiring neither model nor summary features to be differentiable) and gives full flexibility on defining a prior. We illustrated the power of our approach on a diverse set of applications, highlighting the potential of SNPE to rapidly identify data-compatible mechanistic models, to investigate which data-features effectively constrain parameters, and to reveal shortcomings of candidate-models.

Finally, we used a model of the stomatogastric ganglion to show how SNPE can identify complex, high-dimensional parameter landscapes of neural systems. We analyzed the geometrical structure of the parameter landscape and confirmed that circuit configurations need to be finely tuned, even if individual parameters can take on a broad range of values. We showed that different configurations are connected in parameter space, and provided hypotheses for compensation mechanisms. These analyses were made possible by SNPE's ability to estimate full parameter posteriors, rather than just constraints on individual parameters, as is common in many statistical parameter-identification approaches.

Related work

SNPE builds on recent advances in machine learning, and in particular in density-estimation approaches to likelihood-free inference (***Chan et al., 2018***; ***Greenberg et al., 2019***; ***Le et al., 2017b***; ***Lueckmann et al., 2017***; ***Papamakarios and Murray, 2016***), reviewed in ***Cranmer et al.*** (***2019***). We here scaled these approaches to canonical mechanistic models of neural dynamics, and provided methods and software-tools for inference, visualization, and analysis of the resulting posteriors (e.g. the high-probability paths and conditional correlations presented here).

The idea of learning inference networks on simulated data can be traced back to *regression-adjustment* methods in ABC (***Beaumont et al., 2002***; ***Blum and François, 2010***). ***Papamakarios and Murray*** (***2016***) first proposed to use expressive conditional density estimators in the form of deep neural networks (***Bishop, 1994***; ***Papamakarios et al., 2017***), and to optimize them sequentially over multiple rounds with cost-functions derived from Bayesian inference principles. Compared to commonly used rejection-based ABC methods (***Pritchard et al., 1999***; ***Rubin et al., 1984***), such as MCMC-ABC (***Marjoram et al., 2003***), SMC-ABC (***Liepe et al., 2014***; ***Sisson et al., 2007***), Bayesian-Optimization ABC (***Gutmann and Corander, 2016***), or ensemble methods (***Britton et al., 2013***; ***Lawson et al., 2018***), SNPE approaches do not require one to define a distance function in data space. In addition, by leveraging the ability of neural networks to learn informative features, they enable scaling to problems with high-dimensional observations, as are common in neuroscience and other fields in biology. We have illustrated this capability in the context of receptive field estimation, where a convolutional neural network extracts summary features from a 1681 dimensional spike-triggered average. Alternative likelihood-free approaches include *synthetic likelihood* methods (***Costa et al., 2013***; ***Durkan et al., 2018***; ***Lueckmann et al., 2019***; ***Meeds and Welling, 2014***; ***Papamakarios et al., 2019b***; ***Wilkinson, 2014***; ***Wood, 2010***), moment-based approximations of the posterior (***Barthelmé and Chopin, 2014***; ***Schröder et al., 2019***), inference compilation (***Casado et al., 2017***; ***Le et al., 2017a***), and density-ratio estimation (***Hermans et al., 2019***). For some mechanistic models in neuroscience (e.g. for integrate-and-fire neurons), likelihoods can be computed via stochastic numerical approximations (***Chen et al., 2003***; ***Huys and Paninski, 2009***; ***Meliza et al., 2014***) or model-specific analytical approaches (***Hertäg et al., 2012***; ***Huys et al., 2006***; ***Ladenbauer et al., 2018***; ***Pozzorini et al., 2015***; ***René et al., 2019***).

How big is the advance brought by SNPE relative to 'conventional' brute-force approaches that aim to exhaustively explore parameter space? A fundamental difference from grid search approaches that have been applied to neuroscientific models (***Caplan et al., 2014***; ***Prinz et al., 2003***; ***Stringer et al., 2016***) is that SNPE can perform Bayesian inference for *stochastic* models, whereas previous approaches identified parameters whose *deterministic* model-outputs were heuristically "close" to empirical data. Depending on the goal of the analysis, either approach might be preferable. SNPE, and Bayesian inference more generally, is derived for stochastic models. SNPE can, in principle, also be applied to deterministic models, but a rigorous mathematical interpretation or empirical evaluation in this regime is beyond the scope of this study. SNPE also differs conceptually and quantitatively from rejection-ABC, in which random parameters are accepted or rejected based on a distance-criterion. SNPE uses *all* simulations during training instead of rejecting some, learns to identify data features informative about model parameters rather than relying on the user to choose the correct data features and distance metric, and performs considerably better than rejection-ABC, in particular for problems with high-dimensional observations (Fig. 2). Another advantage over grid search and rejection-ABC is that SNPE can 'amortize' inference of parameter posteriors, so that one can quickly perform inference on new data, or explore compensation mechanisms, without having to carry out new simulations, or repeatedly search a simulation database. We should still note that SNPE can require the generation of large sets of simulations, which can be viewed as a brute-force step, emphasising that one of the main strengths of SNPE over conventional brute-force approaches relies on the processing of these simulations via deep neural density estimators.

Our approach is already finding its first applications in neuroscience–for example, ***Oesterle et al.*** (***2020***) have used a variant of SNPE to constrain biophysical models of retinal neurons, with the goal of optimizing stimulation approaches for neuroprosthetics. Concurrently with our work, ***Bittner et al.*** (***2019***) developed an alternative approach to parameter identification for mechanistic models, and showed how it can be used to characterize neural population models which exhibit specific emergent computational properties. Both studies differ in their methodology and domain of applicability (see descriptions of underlying algorithms in our (***Greenberg et al., 2019***; ***Lueckmann et al., 2017***) and their (***Loaiza-Ganem et al., 2017***) prior work), as well in the focus of their neuroscientific contributions. Both approaches share the overall goal of using deep probabilistic inference tools to build more interpretable models of neural data. These complementary and concurrent advances will expedite the cycle of building, adjusting and selecting mechanistic models in neuroscience.

Finally, a complementary approach to mechanistic modeling is to pursue purely phenomenological models, which are designed to have favorable statistical and computational properties: these data-driven models can be efficiently fit to neural data (***Brown et al., 1998***; ***Cunningham and Yu, 2014***; ***Macke et al., 2011***; ***Pandarinath et al., 2018***; ***Pillow, 2007***; ***Pillow et al., 2008***; ***Schneidman et al., 2006***; ***Truccolo et al., 2005***; ***Yu et al., 2009***) or to implement desired computations (***Sussillo and Abbott, 2009***). Although tremendously useful for a quantitative characterization of neural dynamics, these models typically have a large number of parameters, which rarely correspond to physically measurable or mechanistically interpretable quantities, and thus it can be challenging to derive mechanistic insights or causal hypotheses from them (but see e.g. ***Maheswaranathan et al.*** (***2019***); ***Mante et al.*** (***2013***); ***Sussillo and Barak*** (***2013***)).

Use of summary features

When fitting mechanistic models to data, it is common to target summary features to isolate specific behaviors, rather than the full data. For example, the spike shape is known to constrain sodium and potassium conductances (***Druckmann et al., 2007***; ***Hay et al., 2011***; ***Pospischil et al., 2008***). When modeling population dynamics, it is often desirable to achieve realistic firing rates, rate-correlations and response nonlinearities (***Bittner et al., 2019***; ***Rubin et al., 2015***), or specified oscillations (***Prinz et al., 2004***). In models of decision making, one is often interested in reproducing psychometric functions or reaction-time distributions (***Ratcliff and McKoon, 2008***). Choice of summary features might also be guided by known limitations of either the model or the measurement approach, or necessitated by the fact that published data are only available in summarized form. Several methods have been proposed to automatically construct informative summary features (***Blum et al., 2013***; ***Izbicki et al., 2019***; ***Jiang et al., 2017***). SNPE can be applied to, and might benefit from the use of summary features, but it also makes use of the ability of neural networks to automatically learn informative features in high-dimensional data. Thus, SNPE can also be applied directly to raw data (e.g. using recurrent neural networks (***Lueckmann et al., 2017***)), or to high-dimensional summary features which are challenging for ABC approaches (Fig. 2). In all cases, care is needed when interpreting models fit to summary features, as choice of features can influence the results (***Blum et al., 2013***; ***Izbicki et al., 2019***; ***Jiang et al., 2017***).

Applicability and limitations

A key advantage of SNPE is its general applicability: it can be applied whenever one has a simulator that allows to stochastically generate model outputs from specific parameters. Furthermore, it can be applied in a fully 'black-box manner', i.e. does not require access to the internal workings of the simulator, its model equations, likelihoods or gradients. It does not impose any other limitations on the model or the summary features, and in particular does not require them to be differentiable. However, it also has limitations which we enumerate below.

First, current implementations of SNPE scale well to high-dimensional observations ($\sim$1000s dims, also see ***Greenberg et al.*** (***2019***)), but scaling SNPE to even higher-dimensional parameter spaces (>30) is challenging (note that previous approaches were generally limited to dim< 10). Given that the difficulty of estimating full posteriors scales exponentially with dimensionality, this is an inherent challenge for all approaches that aim at full inference (in contrast to just identifying a single, or a few heuristically chosen parameter fits).

Second, while it is a long-term goal for these approaches to be made fully automatic, our current implementation still requires choices by the user: as described in Methods, one needs to choose the type of the density estimation network, and specify settings related to network-optimisation, and the number of simulations and inference rounds. These settings depend on the complexity of the relation between summary features and model parameters, and the number of simulations that can be afforded. In the documentation accompanying our code-package, we provide examples and guidance. For small-scale problems, we have found SNPE to be robust to these settings. However, for challenging, high-dimensional applications, SNPE might currently require substantial user interaction.

Third, the power of SNPE crucially rests on the ability of deep neural networks to perform density estimation. While deep nets have had ample empirical success, we still have an incomplete understanding of their limitations, in particular in cases where the mapping between data and parameters might not be smooth (e.g. near phase transitions).

Fourth, when applying SNPE (or any other model-identification approach), validation of the results is of crucial importance, both to assess the accuracy of the inference procedure, as well as to identify possible limitations of the mechanistic model itself. In the example applications, we used several procedures for assessing the quality of the inferred posteriors. One common ingredient of these approaches is to sample from the inferred model, and search for systematic differences between observed and simulated data, e.g. to perform *posterior predictive checks* (***Cook et al., 2006***; ***Greenberg et al., 2019***; ***Liepe et al., 2014***; ***Lueckmann et al., 2017***; ***Talts et al., 2018***) (Fig. 2g, Fig. 3f,g, Fig. 4c, and Fig. 5d). These approaches allow one to detect 'failures' of SNPE, i.e. cases in which samples from the posterior do not reproduce the data. However, when diagnosing any Bayesian inference approach, it is challenging to rigorously rule out the possibility that additional parameter-settings (e.g. in an isolated 'island') would also explain the data. Thus, it is good practice to use multiple initialisations of SNPE, and/or a large number of simulations in the initial round. There are challenges and opportunities ahead in further scaling and automating simulation-based inference approaches. However, in its current form, SNPE will be a powerful tool for quantitatively evaluating mechanistic hypotheses on neural data, and for designing better models of neural dynamics.

Acknowledgments

We thank Mahmood S. Hoseini and Michael Stryker for sharing their data for Fig. 2, and Philipp Berens, Sean Bittner, Jan Boelts, John Cunningham, Richard Gao, Scott Linderman, Eve Marder, Iain Murray, George Papamakarios, Astrid Prinz, Auguste Schulz and Srinivas Turaga for discussions and/or comments on the manuscript. This work was supported by the German Research Foundation (DFG) through SFB 1233 'Robust Vision', (276693517), SFB 1089 'Synaptic Microcircuits', SPP 2041 'Computational Connectomics' and Germany's Excellence Strategy – EXC-Number 2064/1 – Project number 390727645 and the German Federal Ministry of Education and Research (BMBF, project 'ADIMEM', FKZ 01IS18052 A-D) to JHM, a Sir Henry Dale Fellowship by the Wellcome Trust and the Royal Society (WT100000; WFP and TPV), a Wellcome Trust Senior Research Fellowship (214316/Z/18/Z; TPV), a ERC Consolidator Grant (SYNAPSEEK; WPF and CC), and a UK Research and Innovation, Biotechnology and Biological Sciences Research Council (CC, UKRI-BBSRC BB/N019512/1.

Methods

Code availability

Code implementing SNPE based on Theano, is available at http://www.mackelab.org/delfi/. An extended toolbox based on PyTorch is available at http://www.mackelab.org/sbi/ (***Tejero-Cantero et al., 2020***).

Simulation-based inference

To perform Bayesian parameter identification with SNPE, three types of input need to be specified:

1. A mechanistic model. The model only needs to be specified through a simulator, i.e. that one can generate a simulation result $\mathbf{x}$ for any parameters $\boldsymbol{\theta}$. We do not assume access to the likelihood $p(\mathbf{x}|\boldsymbol{\theta})$ or the equations or internals of the code defining the model, nor do we require the model to be differentiable. This is in contrast to many alternative approaches (including ***Bittner et al.*** (***2019***)), which require the model to be differentiable and to be implemented in a software code that is amenable to automatic differentiation packages. Finally, SNPE can both deal with inputs $\mathbf{x}$ which resemble 'raw' outputs of the model, or summary features calculated from data.
2. Observed data $\mathbf{x}_o$ of the same form as the results $\mathbf{x}$ produced by model simulations.
3. A prior distribution $p(\boldsymbol{\theta})$ describing the range of possible parameters. $p(\boldsymbol{\theta})$ could consist of upper and lower bounds for each parameter, or a more complex distribution incorporating mechanistic first principles or knowledge gained from previous inference procedures on other data. In our applications, we chose priors deemed reasonable or informed by previous studies (see Methods), although setting such priors is an open problem in itself, and outside of the scope of this study.

For each problem, our goal was to estimate the posterior distribution $p(\boldsymbol{\theta}|\mathbf{x}_o)$. To do this we used SNPE (***Greenberg et al., 2019***; ***Lueckmann et al., 2017***; ***Papamakarios and Murray, 2016***). Setting up the inference procedure required three design choices:

1. A network architecture, including number of layers, units per layer, layer type (feedforward or convolutional), activation function and skip connections.
2. A parametric family of probability densities $q_\psi(\boldsymbol{\theta})$ to represent inferred posteriors, to be used as conditional density estimator. We used either a mixture of Gaussians (MoG) or a masked autoregressive flow (MAF) (***Papamakarios et al., 2017***). In the former case, the number of components K must be specified; in the latter the number of *MADES* (Masked Autoencoder for Distribution Estimation) n_{MADES}. Both choices are able to represent richly structured, and multimodal posterior distributions (more details on neural density estimation below).
3. A simulation budget, i.e. number of rounds R and simulations per round N_r. The required number of simulations depends on both the dimensionality and complexity of the function between summary statistics and model parameters. While the number of parameters and summary-features can easily be determined, it can be hard to determine how 'complex' (or nonlinear) this mapping is. This makes it difficult to give general guidelines on how many simulations will be required. A practical approach is to choose a simulation-budget based on the computational cost of the simulation, inspect the results (e.g. with posterior predictive checks), and add more simulations when it seems necessary.

We emphasize that SNPE is highly modular, i.e. that the the inputs (data, the prior over parameter, the mechanistic model), and algorithmic components (network architecture, probability density, optimization approach) can all be modified and chosen independently. This allows neuroscientists to work with models which are designed with mechanistic principles—and not convenience of inference—in mind. Furthermore, it allows SNPE to benefit from advances in more flexible density estimators, more powerful network architectures, or optimization strategies.

With the problem and inference settings specified, SNPE adjusts the network weights ϕ based on simulation results, so that $p(\boldsymbol{\theta}|\mathbf{x}) \approx q_{F(\mathbf{x},\phi)}(\boldsymbol{\theta})$ for any $\mathbf{x}$. In the first round of SNPE simulation parameters are drawn from the prior $p(\boldsymbol{\theta})$. If a single round of inference is not sufficient, SNPE can be run in multiple rounds, in which samples are drawn from the version of $q_{F(\mathbf{x}_o,\phi)}(\boldsymbol{\theta})$ at the beginning of the round. After the last round, $q_{F(\mathbf{x}_o,\phi)}$ is returned as the inferred posterior on parameters $\boldsymbol{\theta}$ given observed data $\mathbf{x}_o$. If SNPE is only run for a single round, then the generated samples only depend on the prior, but not on $\mathbf{x}_o$: in this case, the inference network is applicable to any data (covered by the prior ranges), and can be used for rapid amortized inference.

SNPE learns the correct network weights ϕ by minimizing the objective function $\sum_j \mathcal{L}(\boldsymbol{\theta}_j, \mathbf{x}_j)$ where the simulation with parameters $\boldsymbol{\theta}_j$ produced result $\mathbf{x}_j$. For the first round of SNPE $\mathcal{L}(\boldsymbol{\theta}_j, \mathbf{x}_j) = -\log q_{F(\mathbf{x}_j,\phi)}$, while in subsequent rounds a different loss function accounts for the fact that simulation parameters were not sampled from the prior. Different choices of the loss function for later rounds result in SNPE-A (***Papamakarios and Murray, 2016***), SNPE-B (***Lueckmann et al., 2017***) or SNPE-C algorithm (***Greenberg et al., 2019***). To optimize the networks, we used ADAM with default settings (***Kingma and Ba, 2014***).

The details of the algorithm are below:

Algorithm 1: SNPE

```
Input: simulator with (implicit) density $p(\mathbf{x}|\boldsymbol{\theta})$, observed data $\mathbf{x}_o$, prior $p(\boldsymbol{\theta})$, density family $q_\psi$,
neural network $F(\mathbf{x}, \phi)$, number of rounds $R$, simulation count for each round $N_r$
randomly initialize $\phi$
$\tilde{p}_1(\boldsymbol{\theta}) := p(\boldsymbol{\theta})$
$N := 0$
for $r = 1$ to $R$ do
    for $i = 1 \ldots N_r$ do
        sample $\boldsymbol{\theta}_{N+i} \sim \tilde{p}_r(\boldsymbol{\theta})$
        simulate $\mathbf{x}_{N+i} \sim p(\mathbf{x}|\boldsymbol{\theta}_{N+i})$
    $N \leftarrow N + N_r$
    train $\phi \leftarrow \arg\min_{\phi} \sum_{j=1}^{N} \mathcal{L}(\boldsymbol{\theta}_j, \mathbf{x}_j)$
    $\tilde{p}_r(\boldsymbol{\theta}) := q_{F(\mathbf{x}_o,\phi)}(\boldsymbol{\theta})$
return $q_{F(\mathbf{x}_o,\phi)}(\boldsymbol{\theta})$
```

Bayesian inference without likelihood-evaluations with SNPE

In ***Papamakarios and Murray*** (***2016***), it was shown that the procedure described above (i.e. sample from the prior, train a flexible density estimator by minimizing the log-loss $\mathcal{L}(\boldsymbol{\theta}_j, \mathbf{x}_j) = -\sum_j \log q_{F(\mathbf{x}_j,\phi)}(\boldsymbol{\theta}_j)$) can be used to perform Bayesian inference without likelihood evaluations.

For the multi-round case, in which samples are no longer drawn from the prior, but adaptively generated from a (generally more focused) proposal distribution, the loss function needs to be modified. Different variants of SNPE differ in how exactly this is done:

- SNPE-A minimizes the same loss function as in the first round, but applies a post-hoc analytical correction (***Papamakarios and Murray, 2016***)
- SNPE-B minimizes an importance-weighted loss function, directly approximating the posterior and therefore not requiring a post-hoc correction (***Lueckmann et al., 2017***)
- SNPE-C avoids importance weights (which can have high variance), by either calculating normalization constants in closed-form or using a classifier-based loss (***Greenberg et al., 2019***)

Neural density estimation

As described above, SNPE approximates the posterior distribution with flexible neural density estimators: either a mixture density network (MDN) or a masked autoregressive flow (MAF). Below, we provide a few more details about these density estimators, how we chose their respective architectures, and when to choose one or the other.

The MDN outputs the parameters of a mixture of Gaussians (i.e. mixture weights, and for each component of the mixture, the mean vector and covariance entries). Thus, for an MDN composed of K components, we chose an architecture with at least as many units per layer as $K(1 + dim(\theta) + dim(\theta)(dim(\theta) + 1)/2) - 1$, to ensure enough flexibility to approximate well the parameters of the mixture of Gaussians. For example, when inferring the parameters of the Hodgkin-Huxley model given in vitro recordings from mouse cortex (Allen Cell Types Database, https://celltypes.brain-map.org/data), we infer the posterior over 8 parameters with a mixture of two Gaussians, and the MDN needs at least 89 units per layer. Across applications, we found 2 layers to be sufficient to appropriately approximate the posterior distribution.

MAF is a specific type of normalizing flow, which is a highly flexible density estimator (***Papamakarios et al., 2019a***, ***2017***; ***Rezende and Mohamed, 2015***). Normalizing flows consist of a stack of bijections which transform a simple distribution (usually a multivariate Gaussian distribution) into the target distribution. Each bijection is parameterized by a specific type of neural network (for MAF: a Masked Autoencoder for Distribution Estimation, or MADE). In our experiments, 5 stacked bijections are enough to approximate even complex posterior distributions. Depending on the size of the parameter and data space, each neural network had between [50,50] and [200,400] hidden units.

When using SNPE in a single-round, we generally found superior performance for MAFs as compared to MDNs. When running inference across multiple rounds, training MAFs leads to additional challenges which might impede the quality of inference (***Durkan et al., 2020***; ***Greenberg et al., 2019***).

Linear-nonlinear encoding models

We used a Linear-Nonlinear (LN) encoding model (a special case of a generalized linear model, GLM, (***Brown et al., 1998***; ***Gerwinn et al., 2010***; ***Paninski, 2004***; ***Pillow, 2007***; ***Pillow et al., 2008***; ***Truccolo et al., 2005***)) to simulate the activity of a neuron in response to a univariate time-varying stimulus. Neural activity z_i was subdivided in $T = 100$ bins and, within each bin i, spikes were generated according to a Bernoulli observation model,

$$z_i \sim \mathrm{Bern}(\eta(\mathbf{v}_i^\top \boldsymbol{f} + \beta)),$$

where $\mathbf{v}_i$ is a vector of white noise inputs between time bins $i - 8$ and i, $\boldsymbol{f}$ a length-9 linear filter, β is the bias, and $\eta(\cdot) = \exp(\cdot)/(1 + \exp(\cdot))$ is the canonical inverse link function for a Bernoulli GLM. As summary features, we used the total number of spikes N and the spike-triggered average $\frac{1}{N}\mathbf{Vz}$, where $\mathbf{V} = [v_1, v_2, \ldots, v_T]$ is the so-called design matrix of size $9 \times T$. We note that the spike-triggered sum $\mathbf{Vz}$ constitutes sufficient statistics for this GLM, i.e. that selecting the STA and N together as summary features does not lead to loss of model relevant information over the full input-output dataset $\{\mathbf{V}, \mathbf{z}\}$. We used a Gaussian prior with zero mean and covariance matrix $\boldsymbol{\Sigma} = \sigma^2(\mathbf{F}^\top\mathbf{F})^{-1}$, where $\mathbf{F}$ encourages smoothness by penalizing the second-order differences in the vector of parameters (***De Nicolao et al., 1997***).

For inference, we used a single round of 10000 simulations, and the posterior was approximated with a Gaussian distribution ($\boldsymbol{\theta} \in \mathbb{R}^{10}, \mathbf{x} \in \mathbb{R}^{10}$). We used a feedforward neural network with two hidden layers of 50 units each. We used a Polya Gamma Markov Chain Monte Carlo sampling scheme (***Polson et al., 2013***) to estimate a reference posterior.

In Fig. 2d, we compare the performance of SNPE with two classical ABC algorithms, rejection ABC and Sequential Monte Carlo ABC as a function of the number of simulations. We report the relative error in Kullback-Leibler divergence, which is defined as:

$$\frac{D_{\mathrm{KL}}(p_{MCMC}(\boldsymbol{\theta}|\mathbf{x}) \;||\; \hat{p}(\boldsymbol{\theta}|\mathbf{x}))}{D_{\mathrm{KL}}(p_{MCMC}(\boldsymbol{\theta}|\mathbf{x}) \;||\; p(\boldsymbol{\theta}))}, \tag{1}$$

and which ranges between 0 (perfect recovery of the posterior) and 1 (estimated posterior no better than the prior). Here, $p_{MCMC}(\boldsymbol{\theta}|\mathbf{x})$ is the ground-truth posterior estimated via Markov Chain Monte Carlo sampling, $\hat{p}(\boldsymbol{\theta}|\mathbf{x})$ is the estimated posterior via SNPE, rejection ABC or Sequential Monte Carlo ABC, and $p(\boldsymbol{\theta})$ is the prior.

For the spatial receptive field model of a cell in primary visual cortex, we simulated the activity of a neuron depending on an image-valued stimulus. Neural activity was subdivided in bins of length $\Delta t = 0.025s$ and within each bin i, spikes were generated according to a Poisson observation model,

$$z_i \sim \text{Poiss}(\eta(\mathbf{v}_i^\top \boldsymbol{h} + \beta)),$$

where $\mathbf{v}_i$ is the vectorized white noise stimulus at time bin i, $\boldsymbol{h}$ a 41×41 linear filter, β is the bias, and $\eta(\cdot) = \exp(\cdot)$ is the canonical inverse link function for a Poisson GLM. The receptive field $\boldsymbol{h}$ is constrained to be a Gabor filter:

$$h(g_x, g_y) = g \exp\left(-\frac{x'^2 + r^2 y'^2}{2\sigma^2}\right) \cos\left(2\pi f x' - \phi\right)$$

$$x' = (g_x - x)\cos\psi - (g_y - y)\sin\psi$$

$$y' = (g_x - x)\sin\psi + (g_y - y)\cos\psi$$

$$\sigma = \frac{\sqrt{2}\log 2}{2\pi f}\frac{2^w + 1}{2^w - 1},$$

where (g_x, g_y) is a regular grid of 41×41 positions spanning the 2D image-valued stimulus. The parameters of the Gabor are gain g, spatial frequency f, aspect-ratio r, width w, phase ϕ (between 0 and π), angle ψ (between 0 and 2π) and location x, y (assumed within the stimulated area, scaled to be between -1 and 1). Bounded parameters were transformed with a log-, or logit-transform, to yield unconstrained parameters. After applying SNPE, we back-transformed both the parameters and the estimated posteriors in closed form, as shown in Fig. 2. We did not transform the bias β.

We used a factorizing Gaussian prior for the vector of transformed Gabor parameters

$$[\ \log g,\ \log f,\ \log r,\ \log w,\ l_{0,\pi}(\phi),\ l_{0,2\pi}(\psi),\ l_{-1,1}(x),\ l_{-1,1}(y)\ ],$$

where transforms $l_{0,\pi}(X) = \log(X/(2\pi - X))$, $l_{0,2\pi}(X) = \log(X/(\pi - X))$, $l_{-1,1}(X) = \log((X+1)/(1-X))$ ensured the assumed ranges for the Gabor parameters ϕ, ψ, x, y. Our Gaussian prior had zero mean and standard deviations $[0.5, 0.5, 0.5, 0.5, 1.9, 1.78, 1.78, 1.78]$. We note that a Gaussian prior on a logit-transformed random variable logit$X$ with zero mean and standard deviation around 1.78 is close to a uniform prior over the original variable X. For the bias β, we used a Gaussian prior with mean -0.57 and variance 1.63, which approximately corresponds to an exponential prior $exp(\beta) \sim Exp(\lambda)$ with rate $\lambda = 1$ on the baseline firing rate $\exp(\beta)$ in absence of any stimulus.

The ground-truth parameters for the demonstration in Fig. 2 were chosen to give an asymptotic firing rate of 1Hz for 5 minutes stimulation, resulting in 299 spikes, and a signal-to-noise ratio of -12dB.

As summary features, we used the total number of spikes N and the spike-triggered average $\frac{1}{N}\mathbf{V}\mathbf{z}$, where $\mathbf{V} = [v_1, v_2, \ldots, v_T]$ is the stimulation video of length $T = 300/\Delta t = 12000$. As for the GLM with a temporal filter, the spike-triggered sum $\mathbf{V}\mathbf{z}$ constitutes sufficient statistics for this GLM.

For inference, we applied SNPE-A with in total 2 rounds: an initial round serves to first roughly identify the relevant region of parameter space. Here we used a Gaussian distribution to approximate the posterior from 100000 simulations each. A second round then used a mixture of 8 Gaussian components to estimate the exact shape of the posterior from another 100000 simulations ($\boldsymbol{\theta} \in \mathbb{R}^9, \mathbf{x} \in \mathbb{R}^{1682}$). We used a convolutional network with 5 convolutional layers with 16 to 32 convolutional filters followed by two fully connected layers with 50 units each. The total number of spikes N within a simulated experiment was passed as an additional input directly to the fully-connected layers of the network. Similar to the previous GLM, this model has a tractable likelihood, so we use MCMC to obtain a reference posterior.

We applied this approach to extracelullar recordings from primary visual cortex of alert mice obtained using silicon microelectrodes in response to colored-noise visual stimulation. Experimental methods are described in ***Dyballa et al.*** (***2018***).

Comparison with Sequential Monte Carlo (SMC) ABC

In order to illustrate the competitive performance of SNPE, we obtained a posterior estimate with a classical ABC method, Sequential Monte Carlo (SMC) ABC (***Beaumont et al., 2009***; ***Sisson et al., 2007***). Likelihood-free inference methods from the ABC family require a distance function $d(\mathbf{x}_o, \mathbf{x})$ between observed data $\mathbf{x}_o$ and possible simulation outputs $\mathbf{x}$ to characterize dissimilarity between simulations and data. A common choice is the (scaled) Euclidean distance $d(\mathbf{x}_o, \mathbf{x}) = ||\mathbf{x} - \mathbf{x}_o||_2$. The Euclidean distance here was computed over 1681 summary features given by the spike-triggered average (one per pixel) and a single summary feature given by the 'spike count'. To ensure that the distance measure was sensitive to differences in both STA and spike count, we scaled the summary feature 'spike count' to account for about 20% of the average total distance (other values did not yield better results). The other 80% were computed from the remaining 1681 summary features given by spike-triggered averages.

To showcase how this situation is challenging for ABC approaches, we generated 10000 input-output pairs $(\boldsymbol{\theta}_i, \mathbf{x}_i) \sim p(\mathbf{x}|\boldsymbol{\theta})p(\boldsymbol{\theta})$ with the prior and simulator used above, and illustrate the 10 STAs and spike counts with closest $d(\mathbf{x}_o, \mathbf{x}_i)$ in Supplementary Fig. 5a. Spike counts were comparable to the observed data (299 spikes), but STAs are noise-dominated and the 10 'closest' underlying receptive fields (orange contours) show substantial variability in location and shape of the receptive field. If even the 'closest' samples do not show any visible receptive field, then there is little hope that even an appropriately chosen acceptance threshold will yield a good approximation to the posterior. These findings were also reflected in the results from SMC-ABC with a total simulation budget of 10^6 simulations (Fig. 5b). The estimated posterior marginals for 'bias' and 'gain' parameters show that the parameters related to the firing rate were constrained by the data $\mathbf{x}_o$, but marginals of parameters related to shape and location of the receptive field did not differ from the prior, highlighting that SMC-ABC was not able to identify the posterior distribution. The low correlations between the ground-truth receptive field and receptive fields sampled from SMC-ABC posterior further highlight the failure of SMC-ABC to infer the ground-truth posterior (Fig. 5c). Further comparisons of neural-density estimation approaches with ABC-methods can be found in the studies describing the underlying machine-learning methodologies (***Greenberg et al., 2019***; ***Lueckmann et al., 2019***; ***Papamakarios and Murray, 2016***).

Ion channel models

We simulated non-inactivating potassium channel currents subject to voltage-clamp protocols as:

$$I_K = \bar{g}_{\mathrm{K}} m (V - E_{\mathrm{K}}),$$

where V is the membrane potential, $\bar{g}_{\mathrm{K}}$ is the density of potassium channels, E_{K} is the reversal potential of potassium, and m is the gating variable for potassium channel activation. m is modeled according to the first-order kinetic equation

$$\frac{dm}{dt} = \frac{m_\infty(V) - m}{\tau_m(V)},$$

where $m_\infty(V)$ is the steady-state activation, and $\tau_m(V)$ the respective time constant. We used a general formulation of $m_\infty(V)$ and $\tau_m(V)$ (***Destexhe and Huguenard, 2000***), where the steady-state activation curve has 2 parameters (slope and offset) and the time constant curve has 6 parameters, amounting to a total of 8 parameters (θ_1 to θ_8):

$$m_\infty(V) = \frac{1}{1 + e^{-\theta_1 V + \theta_2}}$$

$$\tau_m(V) = \frac{\theta_4}{e^{-[\theta_5(V-\theta_3) + \theta_6(V-\theta_3)^2]} + e^{[\theta_7(V-\theta_3) + \theta_8(V-\theta_3)^2]}}.$$

Since this model can be used to describe the dynamics of a wide variety of channel models, we refer to it as *Omnimodel*.

We modeled responses of the Omnimodel to a set of five noisy voltage-clamp protocols (***Podlaski et al., 2017***): as described in ***Podlaski et al.*** (***2017***), the original voltage-clamp protocols correspond to standard protocols of activation, inactivation, deactivation, ramp and action potential, to which we added Gaussian noise with zero mean and standard deviation 0.5 mV. Current responses were reduced to 55 summary features (11 per protocol). Summary features were coefficients to basis functions derived via Principal Components Analysis (PCA) (10 per protocol) plus a linear offset (1 per protocol) found via least-squares fitting. PCA basis functions were found by simulating responses of the non-inactivating potassium channel models to the five voltage-clamp protocols and reducing responses to each protocol to 10 dimensions (explaining 99.9% of the variance).

To amortize inference on the model, we specified a wide uniform prior over the parameters: $\theta_1 \in \mathcal{U}(0,1), \theta_2 \in \mathcal{U}(-10., 10.), \theta_3 \in \mathcal{U}(-120., 120.), \theta_4 \in \mathcal{U}(0., 2000), \theta_5 \in \mathcal{U}(0., 0.5), \theta_6 \in \mathcal{U}(0, 0.05), \theta_7 \in \mathcal{U}(0., 0.5), \theta_8 \in \mathcal{U}(0, 0.05)$.

For inference, we trained a shared inference network in a single round of 10^6 simulations generated by sampling from the prior ($\boldsymbol{\theta} \in \mathbb{R}^8, \mathbf{x} \in \mathbb{R}^{55}$). The density estimator is a masked autoregressive flow (MAF) (***Papamakarios et al., 2017***) with five MADES with [250,250] hidden units each.

We evaluated performance on 350 non-inactivating potassium ion channels selected from IonChannelGenealogy (ICG) by calculating the correlation coefficient between traces generated by the original model and traces from the Omnimodel using the posterior mode (Supplementary Fig. 7).

Single-compartment Hodgkin–Huxley neurons

We simulated a single-compartment Hodgkin–Huxley type neuron with channel kinetics as in ***Pospischil et al.*** (***2008***),

$$
\begin{aligned}
C_m \frac{dV}{dt} &= g_{\mathrm{l}}(E_{\mathrm{l}} - V) + \bar{g}_{\mathrm{Na}} m^3 h (E_{\mathrm{Na}} - V) + \bar{g}_{\mathrm{K}} n^4 (E_{\mathrm{K}} - V) + \bar{g}_{\mathrm{M}} p (E_{\mathrm{K}} - V) + I_{\mathrm{inj}} + \sigma \eta(t) \\
\frac{dq}{dt} &= \frac{q_\infty(V) - q}{\tau_q(V)}, q \in \{m, h, n, p\},
\end{aligned}
$$

where V is the membrane potential, C_m is the membrane capacitance, g_{l} is the leak conductance, E_{l} is the membrane reversal potential, $\bar{g}_c$ is the density of channels of type c (Na$^+$, K$^+$, M), E_c is the reversal potential of c, (m, h, n, p) are the respective channel gating kinetic variables, and $\sigma\eta(t)$ is the intrinsic neural Gaussian noise. The right hand side of the voltage dynamics is composed of a leak current, a voltage-dependent Na$^+$ current, a delayed-rectifier K$^+$ current, a slow voltage-dependent K$^+$ current responsible for spike-frequency adaptation, and an injected current I_{inj}. Channel gating variables q have dynamics fully characterized by the neuron membrane potential V, given the respective steady-state $q_\infty(V)$ and time constant $\tau_q(V)$ (details in ***Pospischil et al.*** (***2008***)). Two additional parameters are implicit in the functions $q_\infty(V)$ and $\tau_q(V)$: V_T adjusts the spike threshold through m_∞, h_∞, n_∞, τ_m, τ_h and τ_n; τ_{max} scales the time constant of adaptation through $\tau_p(V)$ (details in ***Pospischil et al.*** (***2008***)). We set $E_{\mathrm{Na}} = 53$ mV and $E_{\mathrm{K}} = -107$ mV, similar to the values used for simulations in Allen Cell Types Database (http://help.brain-map.org/download/attachments/8323525/BiophysModelPeri.pdf).

We applied SNPE to infer the posterior over 8 parameters ($\bar{g}_{\mathrm{Na}}$, $\bar{g}_{\mathrm{K}}$, g_{l}, $\bar{g}_{\mathrm{M}}$, τ_{max}, V_T, σ, E_{l}), given 7 voltage features (number of spikes, mean resting potential, standard deviation of the resting potential, and the first 4 voltage moments, mean, standard deviation, skewness and kurtosis).

The prior distribution over the parameters was uniform,

$$
\boldsymbol{\theta} \sim \mathcal{U}\left(p_{\mathrm{low}}, p_{\mathrm{high}}\right),
$$

where $p_{\mathrm{low}} = [0.5, 10^{-4}, 10^{-4}, 10^{-4}, 50, 40, 10^{-4}, 35]$ and $p_{\mathrm{high}} = [80, 15, 0.6, 0.6, 3000, 90, 0.15, 100]$. These ranges are similar to the ones obtained in ***Pospischil et al.*** (***2008***).

For inference in simulated data, we used a single round of 100000 simulations ($\boldsymbol{\theta} \in \mathbb{R}^8, \mathbf{x} \in \mathbb{R}^{11}$). The density estimator was a masked autoregressive flow (MAF) (**Papamakarios et al., 2017**) with five MADES with [50,50] hidden units each.

For the inference on in vitro recordings from mouse cortex (Allen Cell Types Database, https://celltypes.brain-map.org/data), we selected 8 recordings corresponding to spiny neurons with at least 10 spikes during the current-clamp stimulation. The respective cell identities and sweeps are: (518290966,57), (509881736,39), (566517779,46), (567399060,38), (569469018,44), (532571720,42), (555060623,34), (534524026,29). For each recording, SNPE-B was run for 2 rounds with 125000 Hodgkin–Huxley simulations each, and the posterior was approximated by a mixture of two Gaussians. In this case, the density estimator was composed of two fully connected layers of 100 units each.

Comparison with genetic algorithm

We compared SNPE posterior with a state-of-the-art genetic algorithm (Indicator Based Evolutionary Algorithm IBEA, (**Bleuler et al., 2003**; **Zitzler and Künzli, 2004**) from the BluePyOpt package (**Van Geit et al., 2016**)), in the context of the Hodgkin-Huxley model with 8 parameters and 7 features (Supplementary Fig. 10). For each Hodgkin-Huxley model simulation i and summary feature j, we used the following objective score:

$$\epsilon_{ij} = \left| \frac{x_{ij} - x_{oj}}{\sigma_j} \right|, \; j = 1, ..., 7,$$

where x_{ij} is the value of summary feature j for simulation i, x_{oj} is the observed summary feature j, and σ_j is the standard deviation of the summary feature j computed across 1000 previously simulated datasets. IBEA outputs the hall-of-fame, which corresponds to the 10 parameter sets with the lowest sum of objectives $\sum_j^7 \epsilon_{ij}$. We ran IBEA with 100 generations and an offspring size of 1000 individuals, corresponding to a total of 100000 simulations.

Circuit model of the crustacean stomatogastric ganglion

We used extracellular nerve recordings made from the stomatogastric motor neurons that principally comprise the triphasic pyloric rhythm in the crab *Cancer borealis* (**Haddad and Marder, 2018**). The preparations were decentralized, i.e. the axons of the descending modulatory inputs were severed. The data was recorded at a temperature of 11 °C. See **Haddad and Marder** (**2018**) for full experimental details.

We simulated the circuit model of the crustacean stomatogastric ganglion by adapting a model described in **Prinz et al.** (**2004**). The model is composed of three single-compartment neurons, AB/PD, LP, and PD, where the electrically coupled AB and PD neurons are modeled as a single neuron. Each of the model neurons contains 8 currents, a Na$^+$ current I_{Na}, a fast and a slow transient Ca^{2+} current I_{CaT} and I_{CaS}, a transient K$^+$ current I_{A}, a Ca^{2+}-dependent K$^+$ current I_{KCa}, a delayed rectifier K$^+$ current I_{Kd}, a hyperpolarization-activated inward current I_{H}, and a leak current I_{leak}. In addition, the model contains 7 synapses. As in **Prinz et al.** (**2004**), these synapses were simulated using a standard model of synaptic dynamics (**Abbott and Marder, 1998**). The synaptic input current into the neurons is given by $I_{\text{s}} = g_{\text{s}} s (V_{\text{post}} - E_{\text{s}})$, where g_{s} is the maximal synapse conductance, V_{post} the membrane potential of the postsynaptic neuron, and E_{s} the reversal potential of the synapse. The evolution of the activation variable s is given by

$$\frac{ds}{dt} = \frac{\bar{s}(V_{\text{pre}}) - s}{\tau_s}$$

with

$$\bar{s}(V_{\text{pre}}) = \frac{1}{1 + \exp((V_{\text{th}} - V_{\text{pre}})/\delta)} \quad \text{and} \quad \tau_s = \frac{1 - \bar{s}(V_{\text{pre}})}{k_-}.$$

Here, V_{pre} is the membrane potential of the presynaptic neuron, V_{th} is the half-activation voltage of the synapse, δ sets the slope of the activation curve, and k_- is the rate constant for transmitter-receptor dissociation rate.

As in ***Prinz et al.*** (***2004***), two types of synapses were modeled since AB, LP, and PY are glutamatergic neurons whereas PD is cholinergic. We set $E_s = -70$ mV and $k_- = 1/40$ ms for all glutamatergic synapses and $E_s = -80$ mV and $k_- = 1/100$ ms for all cholinergic synapses. For both synapse types, we set $V_{\text{th}} = -35$ mV and $\delta = 5$ mV.

For each set of membrane and synaptic conductances, we numerically simulated the rhythm for 10 seconds with a step size of 0.025 ms. At each time step, each neuron receives Gaussian noise with mean zero and standard deviation 0.001 mV.ms$^{-0.5}$.

We applied SNPE to infer the posterior over 24 membrane parameters and 7 synaptic parameters, i.e. 31 parameters in total. The 7 synaptic parameters were the maximal conductances g_{s} of all synapses in the circuit, each of which is varied uniformly in logarithmic domain from 0.01 nS to 1000 nS, with an exception of the synapse from AB to LP, which is varied uniformly in logarithmic domain from 0.01 nS to 10000 nS. The membrane parameters were the maximal membrane conductances for each of the neurons. The membrane conductances were varied over an extended range of previously reported values (***Prinz et al., 2004***), which led us to the uniform prior bounds $p_{\text{low}} = [0, 0, 0, 0, 0, 25, 0, 0]$ mS cm^{-2} and $p_{\text{high}} = [500, 7.5, 8, 60, 15, 150, 0.2, 0.01]$ mS cm^{-2} for the maximal membrane conductances of the AB neuron, $p_{\text{low}} = [0, 0, 2, 10, 0, 0, 0, 0.01]$ mS cm^{-2} and $p_{\text{high}} = [200, 2.5, 12, 60, 10, 125, 0.06, 0.04]$ mS cm^{-2} for the maximal membrane conductances of the LP neuron, and $p_{\text{low}} = [0, 0, 0, 30, 0, 50, 0, 0]$ mS cm^{-2} and $p_{\text{high}} = [600, 12.5, 4, 60, 5, 150, 0.06, 0.04]$ mS cm^{-2} for the maximal membrane conductances of the PY neuron. The order of the membrane currents was: [Na, CaT, CaS, A, KCa, Kd, H, leak].

We used the 15 summary features proposed by ***Prinz et al.*** (***2004***), and extended them by 3 additional features. The features proposed by ***Prinz et al.*** (***2004***) are 15 salient features of the pyloric rhythm, namely: cycle period T (s), AB/PD burst duration d^{b}_{AB} (s), LP burst duration d^{b}_{LP} (s), PY burst duration d^{b}_{PY} (s), gap AB/PD end to LP start $\Delta t^{\text{es}}_{\text{AB-LP}}$ (s), gap LP end to PY start $\Delta t^{\text{es}}_{\text{LP-PY}}$ (s), delay AB/PD start to LP start $\Delta t^{\text{ss}}_{\text{AB-LP}}$ (s), delay LP start to PY start $\Delta t^{\text{ss}}_{\text{LP-PY}}$ (s), AB/PD duty cycle d_{AB}, LP duty cycle d_{LP}, PY duty cycle d_{PY}, phase gap AB/PD end to LP start $\Delta\phi_{\text{AB-LP}}$, phase gap LP end to PY start $\Delta\phi_{\text{LP-PY}}$, LP start phase ϕ_{LP}, and PY start phase ϕ_{PY}. Note that several of these values are only defined if each neuron produces rhythmic bursting behavior. In addition, for each of the three neurons, we used one feature that describes the maximal duration of its voltage being above -30 mV. We did this as we observed plateaus at around -10 mV during the onset of bursts, and wanted to distinguish such activity traces from others. If the maximal duration was below 5 ms, we set this feature to 5 ms. To extract the summary features from the observed experimental data, we first found spikes by searching for local maxima above a hand-picked voltage threshold, and then extracted the 15 above described features. We set the additional 3 features to 5 ms.

We used SNPE to infer the posterior distribution over the 18 summary features from experimental data. For inference, we used a single round with 18.5 million samples, out of which 174,000 samples contain bursts in all neurons. We therefore used these 174,000 samples with well defined summary features for training the inference network ($\boldsymbol{\theta} \in \mathbb{R}^{31}, \mathbf{x} \in \mathbb{R}^{18}$). The density estimator was a masked autoregressive flow (MAF) (***Papamakarios et al., 2017***) with five MADES with [200,400] hidden units each. The synaptic conductances were transformed into logarithmic space before training and for the entire analysis.

Previous approaches for fitting the STG circuit (***Prinz et al., 2004***) first fit individual neuron features and reduce the number of possible neuron models (***Prinz et al., 2003***), and then fit the whole circuit model. While powerful, this approach both requires the availability of single-neuron data, and cannot give access to potential compensation mechanisms between single-neuron and synaptic parameters. Unlike ***Prinz et al.*** (***2004***), we apply SNPE to directly identify the full 31 dimensional parameter space without requiring experimental measurements of each individual neuron in the circuit. Despite the high-dimensional parameter space, SNPE can identify the posterior distribution using 18 million samples, whereas a direct application of a full-grid method would require $4.65 \cdot 10^{21}$ samples to fill the 31 dimensional parameter space on a grid with five values per dimension.

Finding paths in the posterior

In order to find directions of robust network output, we searched for a path of high posterior probability. First, as in ***Prinz et al.*** (***2004***), we aimed to find 2 similar model outputs with disparate parameters. To do so, we sampled from the posterior and searched for 2 parameter sets whose summary features were within 0.1 standard deviations of all 174,000 samples from the observed experimental data, but that had strongly disparate parameters from each other. In the following, we denote the obtained parameter sets by $\boldsymbol{\theta}_s$ and $\boldsymbol{\theta}_g$.

Second, in order to identify whether network output can be maintained along a continuous path between these 2 samples, we searched for a connection in parameter space lying in regions of high posterior probability. To do so, we considered the connection between the samples as a path and minimize the following path integral:

$$\mathcal{L}(\gamma) = \int_0^1 -\log(p_{\boldsymbol{\theta}|\mathbf{x}}(\gamma(s))|\mathbf{x}_o)\, \|\dot{\gamma}(s)\|\, ds. \qquad (2)$$

To minimize this term, we parameterized the path $\gamma(s)$ using sinusoidal basis-functions with coefficients $\alpha_{n,k}$:

$$\gamma(s) = \begin{bmatrix} \sum_{k=1}^{K} \alpha_{1,k} \cdot \sin(\pi k s) \\ \vdots \\ \sum_{k=1}^{K} \alpha_{N,k} \cdot \sin(\pi k s) \end{bmatrix} + \begin{bmatrix} \sum_{k=K+1}^{2K} \alpha_{1,k} \cdot \sin^2(\pi k s) \\ \vdots \\ \sum_{k=K+1}^{2K} \alpha_{N,k} \cdot \sin^2(\pi k s) \end{bmatrix} + (1-s) \cdot \boldsymbol{\theta}_s + s\boldsymbol{\theta}_g$$

These basis functions are defined such that, for any coefficients $\alpha_{n,k}$, the start and end points of the path are exactly the two parameter sets defined above:

$$\gamma(0) = \boldsymbol{\theta}_s \qquad \gamma(1) = \boldsymbol{\theta}_g$$

With this formulation, we have framed the problem of finding the path as an unconstrained optimization problem over the parameters $\alpha_{n,k}$. We can therefore minimize the path integral L using gradient descent over $\alpha_{n,k}$. For numerical simulations, we approximated the integral in equation 2 as a sum over 80 points along the path and use 2 basis functions for each of the 31 dimensions, i.e. $K = 2$.

In order to demonstrate the sensitivity of the pyloric network, we aimed to find a path along which the circuit output quickly breaks down. For this, we picked a starting point along the high-probability path and then minimized the posterior probability. In addition, we enforced that the orthogonal path lies within an orthogonal disk to the high-probability path, leading to the following constrained optimization problem:

$$\min_{\boldsymbol{\theta}} \log(p(\boldsymbol{\theta}|\mathbf{x})) \qquad \text{s.t.} \quad n^T \Delta\boldsymbol{\theta} = 0$$

where n is the tangent vector along the path of high probability. This optimization problem can be solved using the gradient projection method (***Rosen, 1960***):

$$\Delta\boldsymbol{\theta} = -\frac{P(\nabla \log(p(\boldsymbol{\theta}|\mathbf{x})))}{\sqrt{(\nabla \log(p(\boldsymbol{\theta}|\mathbf{x})))^T P(\nabla \log(p(\boldsymbol{\theta}|\mathbf{x})))}}$$

with projection matrix $P = \mathbb{1} - \frac{1}{n^T n} n n^T$ and $\mathbb{1}$ indicating the identity matrix. Each gradient update is a step along the orthogonal path. We let the optimization run until the distance along the path is $1/27$ of the distance along the high-probability path.

Identifying conditional correlations

In order to investigate compensation mechanisms in the STG, we compared marginal and conditional correlations. For the marginal correlation matrix in Fig. 6b, we calculated the Pearson correlation coefficient based on 1.26 million samples from the posterior distribution $p(\boldsymbol{\theta}|\mathbf{x})$. To find the 2-dimensional conditional distribution for any pair of parameters, we fixed all other parameters to values taken from an arbitrary posterior sample, and varied the remaining 2 on an evenly spaced grid with 50 points along each dimension, covering the entire prior space. We evaluated the posterior distribution at every value on this grid. We then calculated the conditional correlation as the Pearson correlation coefficient over this distribution. For the 1-dimensional conditional distribution, we varied only 1 parameter and kept all others fixed. Lastly, in Fig. 6d, we sampled 500 parameter sets from the posterior, computed the respective conditional posteriors and conditional correlation matrices, and took the average over the conditional correlation matrices.

References

Abbott, L. and Marder, E. (1998). Modeling small networks.

Achard, P. and De Schutter, E. (2006). Complex parameter landscape for a complex neuron model. *PLoS Computational Biology*, 2(7):e94.

Allen Institute for Brain Science (2016). Allen cell types database. http://celltypes.brain-map.org/.

Alonso, L. M. and Marder, E. (2019). Visualization of currents in neural models with similar behavior and different conductance densities. *eLife*, 8:e42722.

Baker, R. E., Pena, J.-M., Jayamohan, J., and Jérusalem, A. (2018). Mechanistic models versus machine learning, a fight worth fighting for the biological community? *Biology Letters*, 14(5).

Barthelmé, S. and Chopin, N. (2014). Expectation propagation for likelihood-free inference. *Journal of the American Statistical Association*, 109(505):315–333.

Bassett, D. S., Zurn, P., and Gold, J. I. (2018). On the nature and use of models in network neuroscience. *Nature Reviews Neuroscience*, 19(9):566.

Beaumont, M., Zhang, W., and Balding, D. J. (2002). Approximate bayesian computation in population genetics. *Genetics*, 162(4).

Beaumont, M. A., Cornuet, J., Marin, J., and Robert, C. P. (2009). Adaptive approximate bayesian computation. *Biometrika*.

Ben-Shalom, R., Balewski, J., Siththaranjan, A., Baratham, V., Kyoung, H., Kim, K. G., Bender, K. J., and Bouchard, K. E. (2019). Inferring neuronal ionic conductances from membrane potentials using cnns. *bioRxiv*.

Bishop, C. M. (1994). Mixture density networks. *Technical Report. Aston University, Birmingham*.

Bittner, S. R., Palmigiano, A., Piet, A. T., Duan, C. A., Brody, C. D., Miller, K. D., and Cunningham, J. P. (2019). Interrogating theoretical models of neural computation with deep inference. *bioRxiv*.

Bleuler, S., Laumanns, M., Thiele, L., and Zitzler, E. (2003). Pisa—a platform and programming language independent interface for search algorithms. In *International Conference on Evolutionary Multi-Criterion Optimization*, pages 494–508. Springer.

Blum, M. G. and François, O. (2010). Non-linear regression models for approximate bayesian computation. *Statistics and Computing*, 20(1):63–73.

Blum, M. G. B., Nunes, M. A., Prangle, D., Sisson, S. A., et al. (2013). A comparative review of dimension reduction methods in approximate bayesian computation. *Statistical Science*, 28(2).

Brette, R. (2015). What is the most realistic single-compartment model of spike initiation? *PLoS Computational Biology*, 11(4):e1004114.

Britton, O. J., Bueno-Orovio, A., Van Ammel, K., Lu, H. R., Towart, R., Gallacher, D. J., and Rodriguez, B. (2013). Experimentally calibrated population of models predicts and explains intersubject variability in cardiac cellular electrophysiology. *Proceedings of the National Academy of Sciences*, 110(23):E2098–E2105.

Brown, E. N., Frank, L. M., Tang, D., Quirk, M. C., and Wilson, M. A. (1998). A statistical paradigm for neural spike train decoding applied to position prediction from ensemble firing patterns of rat hippocampal place cells. *Journal of Neuroscience*, 18(18):7411–7425.

Caplan, J. S., Williams, A. H., and Marder, E. (2014). Many parameter sets in a multicompartment model oscillator are robust to temperature perturbations. *Journal of Neuroscience*, 34(14):4963–4975.

Casado, M. L., Baydin, A. G., Rubio, D. M., Le, T. A., Wood, F., Heinrich, L., Louppe, G., Cranmer, K., Ng, K., Bhimji, W., et al. (2017). Improvements to inference compilation for probabilistic programming in large-scale scientific simulators. *NeurIPS Workshop on Deep Learning for Physical Sciences*.

Chan, J., Perrone, V., Spence, J., Jenkins, P., Mathieson, S., and Song, Y. (2018). A likelihood-free inference framework for population genetic data using exchangeable neural networks. In *Advances in Neural Information Processing Systems*, pages 8594–8605.

Chen, Z. et al. (2003). Bayesian filtering: From kalman filters to particle filters, and beyond. *Statistics*, 182(1):1–69.

Chichilnisky, E. (2001). A simple white noise analysis of neuronal light responses. *Network: Computation in Neural Systems*, 12(2):199–213.

Cook, S. R., Gelman, A., and Rubin, D. B. (2006). Validation of software for bayesian models using posterior quantiles. *Journal of Computational and Graphical Statistics*, 15(3):675–692.

Costa, R. P., Sjostrom, P. J., and Van Rossum, M. C. (2013). Probabilistic inference of short-term synaptic plasticity in neocortical microcircuits. *Frontiers in Computational Neuroscience*, 7:75.

Cranmer, K., Brehmer, J., and Louppe, G. (2019). The frontier of simulation-based inference. *arXiv preprint arXiv:1911.01429*.

Cunningham, J. P. and Yu, B. M. (2014). Dimensionality reduction for large-scale neural recordings. *Nature Neuroscience*, 17(11):1500.

Daly, A. C., Gavaghan, D. J., Holmes, C., and Cooper, J. (2015). Hodgkin–huxley revisited: reparametrization and identifiability analysis of the classic action potential model with approximate bayesian methods. *Royal Society Open Science*, 2(12):150499.

De Nicolao, G., Sparacino, G., and Cobelli, C. (1997). Nonparametric input estimation in physiological systems: problems, methods, and case studies. *Automatica*, 33(5).

Destexhe, A. and Huguenard, J. R. (2000). Nonlinear Thermodynamic Models of Voltage-Dependent Currents. *Journal of Computational Neuroscience*, 9(3):259–270.

Druckmann, S., Banitt, Y., Gidon, A. A., Schürmann, F., Markram, H., and Segev, I. (2007). A novel multiple objective optimization framework for constraining conductance-based neuron models by experimental data. *Frontiers in Neuroscience*, 1:1.

Dunlop, J., Bowlby, M., Peri, R., Vasilyev, D., and Arias, R. (2008). High-throughput electrophysiology: an emerging paradigm for ion-channel screening and physiology. *Nature Reviews Drug Discovery*, 7(4):358.

Durkan, C., Murray, I., and Papamakarios, G. (2020). On contrastive learning for likelihood-free inference. *International Conference on Machine Learning*.

Durkan, C., Papamakarios, G., and Murray, I. (2018). Sequential neural methods for likelihood-free inference. *NeurIPS Bayesian Deep Learning Workshop*.

Dyballa, L., Hoseini, M. S., Dadarlat, M. C., Zucker, S. W., and Stryker, M. P. (2018). Flow stimuli reveal ecologically appropriate responses in mouse visual cortex. *Proceedings of the National Academy of Sciences*, 115(44):11304–11309.

Fisher, D., Olasagasti, I., Tank, D. W., Aksay, E. R., and Goldman, M. S. (2013). A modeling framework for deriving the structural and functional architecture of a short-term memory microcircuit. *Neuron*, 79(5):987–1000.

Foster, W., Ungar, L., and Schwaber, J. (1993). Significance of conductances in hodgkin-huxley models. *Journal of neurophysiology*, 70(6):2502–2518.

Gerstner, W., Sprekeler, H., and Deco, G. (2012). Theory and simulation in neuroscience. *Science*, 338(6103):60–65.

Gerwinn, S., Macke, J. H., and Bethge, M. (2010). Bayesian inference for generalized linear models for spiking neurons. *Frontiers in Computational Neuroscience*, 4:12.

Gold, J. I. and Shadlen, M. N. (2007). The neural basis of decision making. *Annual Review of Neuroscience*, 30.

Goldman, M. S., Golowasch, J., Marder, E., and Abbott, L. (2001). Global structure, robustness, and modulation of neuronal models. *Journal of Neuroscience*, 21(14):5229–5238.

Golowasch, J., Goldman, M. S., Abbott, L., and Marder, E. (2002). Failure of averaging in the construction of a conductance-based neuron model. *Journal of neurophysiology*, 87(2):1129–1131.

Gouwens, N. W., Berg, J., Feng, D., Sorensen, S. A., Zeng, H., Hawrylycz, M. J., Koch, C., and Arkhipov, A. (2018). Systematic generation of biophysically detailed models for diverse cortical neuron types. *Nature Communications*, 9(1):710.

Grashow, R., Brookings, T., and Marder, E. (2010). Compensation for variable intrinsic neuronal excitability by circuit-synaptic interactions. *Journal of Neuroscience*, 30(27):9145–9156.

Greenberg, D., Nonnenmacher, M., and Macke, J. (2019). Automatic posterior transformation for likelihood-free inference. In *International Conference on Machine Learning*, pages 2404–2414.

Gutenkunst, R. N., Waterfall, J. J., Casey, F. P., Brown, K. S., Myers, C. R., and Sethna, J. P. (2007). Universally sloppy parameter sensitivities in systems biology models. *PLoS Computational Biology*, 3(10):e189.

Gutierrez, G. J., O'Leary, T., and Marder, E. (2013). Multiple mechanisms switch an electrically coupled, synaptically inhibited neuron between competing rhythmic oscillators. *Neuron*, 77(5):845–858.

Gutmann, M. U. and Corander, J. (2016). Bayesian optimization for likelihood-free inference of simulator-based statistical models. *The Journal of Machine Learning Research*, 17(1):4256–4302.

Haddad, S. A. and Marder, E. (2018). Circuit robustness to temperature perturbation is altered by neuromodulators. *Neuron*, 100(3):609–623.

Hay, E., Hill, S., Schürmann, F., Markram, H., and Segev, I. (2011). Models of neocortical layer 5b pyramidal cells capturing a wide range of dendritic and perisomatic active properties. *PLoS Computational Biology*, 7(7).

Hermans, J., Begy, V., and Louppe, G. (2019). Likelihood-free mcmc with approximate likelihood ratios. *arXiv preprint arXiv:1903.04057*.

Hertäg, L., Hass, J., Golovko, T., and Durstewitz, D. (2012). An approximation to the adaptive exponential integrate-and-fire neuron model allows fast and predictive fitting to physiological data. *Frontiers in Computational Neuroscience*, 6:62.

Herz, A. V., Gollisch, T., Machens, C. K., and Jaeger, D. (2006a). Modeling single-neuron dynamics and computations: a balance of detail and abstraction. *Science*, 314(5796):80–85.

Herz, A. V. M., Gollisch, T., Machens, C. K., and Jaeger, D. (2006b). Modeling single-neuron dynamics and computations: a balance of detail and abstraction. *Science*, 314(5796).

Hodgkin, A. L. and Huxley, A. F. (1952). A quantitative description of membrane current and its application to conduction and excitation in nerve. *The Journal of Physiology*, 117(4):500–544.

Huys, Q. J. M., Ahrens, M. B., and Paninski, L. (2006). Efficient estimation of detailed single-neuron models. *Journal of Neurophysiology*, 96(2).

Huys, Q. J. M. and Paninski, L. (2009). Smoothing of, and parameter estimation from, noisy biophysical recordings. *PLoS Computational Biology*, 5(5).

Izbicki, R., Lee, A. B., and Pospisil, T. (2019). Abc–cde: Toward approximate bayesian computation with complex high-dimensional data and limited simulations. *Journal of Computational and Graphical Statistics*, pages 1–20.

Jiang, B., Wu, T.-y., Zheng, C., and Wong, W. H. (2017). Learning summary statistic for approximate bayesian computation via deep neural network. *Statistica Sinica*, pages 1595–1618.

Jones, J. P. and Palmer, L. A. (1987). An evaluation of the two-dimensional gabor filter model of simple receptive fields in cat striate cortex. *Journal of Neurophysiology*, 58(6):1233–1258.

Kingma, D. P. and Ba, J. (2014). Adam: A method for stochastic optimization. In *International Conference on Learning Representations*.

Kitano, H. (2004). Biological robustness. *Nature Reviews Genetics*, 5(11):826–837.

Kleinegesse, S. and Gutmann, M. U. (2019). Efficient bayesian experimental design for implicit models. In *The 22nd International Conference on Artificial Intelligence and Statistics*, pages 476–485.

Krizhevsky, A., Sutskever, I., and Hinton, G. E. (2012). Imagenet classification with deep convolutional neural networks. In *Advances in Neural Information Processing Systems*, pages 1097–1105.

Ladenbauer, J., McKenzie, S., English, D. F., Hagens, O., and Ostojic, S. (2018). Inferring and validating mechanistic models of neural microcircuits based on spike-train data. *bioRxiv*, page 261016.

Lawson, B. A., Drovandi, C. C., Cusimano, N., Burrage, P., Rodriguez, B., and Burrage, K. (2018). Unlocking data sets by calibrating populations of models to data density: A study in atrial electrophysiology. *Science Advances*, 4(1):e1701676.

Le, T. A., Baydin, A. G., and Wood, F. (2017a). Inference compilation and universal probabilistic programming. In *Artificial Intelligence and Statistics*, pages 1338–1348.

Le, T. A., Baydin, A. G., Zinkov, R., and Wood, F. (2017b). Using synthetic data to train neural networks is model-based reasoning. In *2017 International Joint Conference on Neural Networks (IJCNN)*, pages 3514–3521. IEEE.

Liepe, J., Kirk, P., Filippi, S., Toni, T., Barnes, C. P., and Stumpf, M. P. (2014). A framework for parameter estimation and model selection from experimental data in systems biology using approximate bayesian computation. *Nature Protocols*, 9(2):439.

Litwin-Kumar, A. and Doiron, B. (2012). Slow dynamics and high variability in balanced cortical networks with clustered connections. *Nature Neuroscience*, 15(11):1498.

Loaiza-Ganem, G., Gao, Y., and Cunningham, J. P. (2017). Maximum entropy flow networks. In *5th International Conference on Learning Representations, ICLR*.

Lueckmann, J.-M., Bassetto, G., Karaletsos, T., and Macke, J. H. (2019). Likelihood-free inference with emulator networks. In Ruiz, F., Zhang, C., Liang, D., and Bui, T., editors, *Proceedings of The 1st Symposium on Advances in Approximate Bayesian Inference*, volume 96 of *Proceedings of Machine Learning Research*, pages 32–53.

Lueckmann, J.-M., Goncalves, P. J., Bassetto, G., Öcal, K., Nonnenmacher, M., and Macke, J. H. (2017). Flexible statistical inference for mechanistic models of neural dynamics. In *Advances in Neural Information Processing Systems*, pages 1289–1299.

Machta, B. B., Chachra, R., Transtrum, M. K., and Sethna, J. P. (2013). Parameter space compression underlies emergent theories and predictive models. *Science*, 342(6158):604–607.

Macke, J. H., Buesing, L., Cunningham, J. P., Yu, B. M., Shenoy, K. V., and Sahani, M. (2011). Empirical models of spiking in neural populations. In *Advances in Neural Information Processing Systems*, pages 1350–1358.

MacLean, J. N., Zhang, Y., Goeritz, M. L., Casey, R., Oliva, R., Guckenheimer, J., and Harris-Warrick, R. M. (2005). Activity-independent coregulation of ia and ih in rhythmically active neurons. *Journal of Neurophysiology*, 94(5):3601–3617.

MacLean, J. N., Zhang, Y., Johnson, B. R., and Harris-Warrick, R. M. (2003). Activity-independent homeostasis in rhythmically active neurons. *Neuron*, 37(1):109–120.

Maheswaranathan, N., Williams, A., Golub, M. D., Ganguli, S., and Sussillo, D. (2019). Reverse engineering recurrent networks for sentiment classification reveals line attractor dynamics. *arXiv preprint arXiv:1906.10720*.

Mante, V., Sussillo, D., Shenoy, K. V., and Newsome, W. T. (2013). Context-dependent computation by recurrent dynamics in prefrontal cortex. *Nature*, 503(7474):78.

Marder, E. (2011). Variability, compensation, and modulation in neurons and circuits. *Proceedings of the National Academy of Sciences*, 108(Supplement 3):15542–15548.

Marder, E. and Goaillard, J.-M. (2006). Variability, compensation and homeostasis in neuron and network function. *Nature Reviews Neuroscience*, 7(7):563.

Marder, E., Goeritz, M. L., and Otopalik, A. G. (2015). Robust circuit rhythms in small circuits arise from variable circuit components and mechanisms. *Current Opinion in Neurobiology*, 31:156–163.

Marder, E. and Taylor, A. L. (2011). Multiple models to capture the variability in biological neurons and networks. *Nature Neuroscience*, 14(2):133.

Marjoram, P., Molitor, J., Plagnol, V., and Tavare, S. (2003). Markov chain monte carlo without likelihoods. *Proceedings of the National Academy of Sciences*, 100(26).

McTavish, T. S., Migliore, M., Shepherd, G. M., and Hines, M. L. (2012). Mitral cell spike synchrony modulated by dendrodendritic synapse location. *Frontiers in computational neuroscience*, 6:3.

Meeds, E. and Welling, M. (2014). Gps-abc: Gaussian process surrogate approximate bayesian computation. In *Conference on Uncertainty in Artificial Intelligence*.

Meliza, C. D., Kostuk, M., Huang, H., Nogaret, A., Margoliash, D., and Abarbanel, H. D. (2014). Estimating parameters and predicting membrane voltages with conductance-based neuron models. *Biological Cybernetics*, 108(4):495–516.

Niell, C. M. and Stryker, M. P. (2008). Highly selective receptive fields in mouse visual cortex. *Journal of Neuroscience*, 28(30):7520–7536.

Oesterle, J., Behrens, C., Schroeder, C., Herrmann, T., Euler, T., Franke, K., Smith, R. G., Zeck, G., and Berens, P. (2020). Bayesian inference for biophysical neuron models enables stimulus optimization for retinal neuroprosthetics. *bioRxiv*.

O'Leary, T. (2018). Homeostasis, failure of homeostasis and degenerate ion channel regulation. *Current Opinion in Physiology*, 2:129–138.

O'Leary, T. and Marder, E. (2016). Temperature-robust neural function from activity-dependent ion channel regulation. *Current Biology*, 26(21):2935–2941.

O'Leary, T., Sutton, A. C., and Marder, E. (2015). Computational models in the age of large datasets. *Current Opinion in Neurobiology*, 32:87–94.

O'Leary, T., Williams, A. H., Franci, A., and Marder, E. (2014). Cell types, network homeostasis, and pathological compensation from a biologically plausible ion channel expression model. *Neuron*, 82(4):809–821.

Pandarinath, C., O'Shea, D. J., Collins, J., Jozefowicz, R., Stavisky, S. D., Kao, J. C., Trautmann, E. M., Kaufman, M. T., Ryu, S. I., Hochberg, L. R., et al. (2018). Inferring single-trial neural population dynamics using sequential autoencoders. *Nature Methods*, page 1.

Paninski, L. (2004). Maximum likelihood estimation of cascade point-process neural encoding models. *Network: Computation in Neural Systems*, 15(4):243–262.

Papamakarios, G. and Murray, I. (2016). Fast ϵ-free inference of simulation models with bayesian conditional density estimation. In *Advances in Neural Information Processing Systems*, pages 1028–1036.

Papamakarios, G., Nalisnick, E., Rezende, D. J., Mohamed, S., and Lakshminarayanan, B. (2019a). Normalizing flows for probabilistic modeling and inference. *arXiv preprint arXiv:1912.02762*.

Papamakarios, G., Pavlakou, T., and Murray, I. (2017). Masked autoregressive flow for density estimation. In *Advances in Neural Information Processing Systems*, pages 2338–2347.

Papamakarios, G., Sterratt, D., and Murray, I. (2019b). Sequential neural likelihood: Fast likelihood-free inference with autoregressive flows. In *The 22nd International Conference on Artificial Intelligence and Statistics*, pages 837–848.

Pillow, J. (2007). Likelihood-based approaches to modeling the neural code. *Bayesian Brain: Probabilistic Approaches to Neural Coding*, pages 53–70.

Pillow, J. W., Paninski, L., Uzzell, V. J., Simoncelli, E. P., and Chichilnisky, E. (2005). Prediction and decoding of retinal ganglion cell responses with a probabilistic spiking model. *Journal of Neuroscience*, 25(47):11003–11013.

Pillow, J. W. and Scott, J. (2012). Fully bayesian inference for neural models with negative-binomial spiking. In *Advances in Neural Information Processing Systems*, pages 1898–1906.

Pillow, J. W., Shlens, J., Paninski, L., Sher, A., Litke, A. M., Chichilnisky, E. J., and Simoncelli, E. P. (2008). Spatio-temporal correlations and visual signalling in a complete neuronal population. *Nature*, 454(7207).

Podlaski, W. F., Seeholzer, A., Groschner, L. N., Miesenböck, G., Ranjan, R., and Vogels, T. P. (2017). Mapping the function of neuronal ion channels in model and experiment. *eLife*, 6:e22152.

Polson, N. G., Scott, J. G., and Windle, J. (2013). Bayesian inference for logistic models using pólya–gamma latent variables. *Journal of the American statistical Association*, 108(504):1339–1349.

Pospischil, M., Toledo-Rodriguez, M., Monier, C., Piwkowska, Z., Bal, T., Frégnac, Y., Markram, H., and Destexhe, A. (2008). Minimal hodgkin-huxley type models for different classes of cortical and thalamic neurons. *Biological Cybernetics*, 99(4-5).

Potjans, T. C. and Diesmann, M. (2012). The cell-type specific cortical microcircuit: relating structure and activity in a full-scale spiking network model. *Cerebral Cortex*, 24(3):785–806.

Pozzorini, C., Mensi, S., Hagens, O., Naud, R., Koch, C., and Gerstner, W. (2015). Automated high-throughput characterization of single neurons by means of simplified spiking models. *PLoS Computational Biology*, 11(6):e1004275.

Prinz, A. A., Billimoria, C. P., and Marder, E. (2003). Alternative to hand-tuning conductance-based models: construction and analysis of databases of model neurons. *Journal of Neurophysiology*, 90(6):3998–4015.

Prinz, A. A., Bucher, D., and Marder, E. (2004). Similar network activity from disparate circuit parameters. *Nature Neuroscience*, 7(12):1345.

Pritchard, J. K., Seielstad, M. T., Perez-Lezaun, A., and Feldman, M. W. (1999). Population growth of human y chromosomes: a study of y chromosome microsatellites. *Molecular Biology and Evolution*, 16(12):1791–1798.

Ranjan, R., Logette, E., Marani, M., Herzog, M., Tache, V., and Markram, H. (2019). A kinetic map of the homomeric voltage-gated potassium channel (kv) family. *Frontiers in Cellular Neuroscience*, 13:358.

Ratcliff, R. and McKoon, G. (2008). The diffusion decision model: theory and data for two-choice decision tasks. *Neural Computation*, 20(4):873–922.

René, A., Longtin, A., and Macke, J. H. (2019). Inference of a mesoscopic population model from population spike trains. *arXiv preprint arXiv:1910.01618*.

Rezende, D. J. and Mohamed, S. (2015). Variational inference with normalizing flows. In *Proceedings of the 32nd International Conference on International Conference on Machine Learning-Volume 37*, pages 1530–1538. JMLR. org.

Rosen, J. B. (1960). The gradient projection method for nonlinear programming. part i. linear constraints. *Journal of the Society for Industrial and Applied Mathematics*, 8(1):181–217.

Rossant, C., Goodman, D. F. M., Fontaine, B., Platkiewicz, J., Magnusson, A. K., and Brette, R. (2011). Fitting neuron models to spike trains. *Frontiers in Neuroscience*, 5:9.

Rubin, D. B. et al. (1984). Bayesianly justifiable and relevant frequency calculations for the applied statistician. *The Annals of Statistics*, 12(4):1151–1172.

Rubin, D. B., Van Hooser, S. D., and Miller, K. D. (2015). The stabilized supralinear network: a unifying circuit motif underlying multi-input integration in sensory cortex. *Neuron*, 85(2):402–417.

Schneidman, E., Berry II, M. J., Segev, R., and Bialek, W. (2006). Weak pairwise correlations imply strongly correlated network states in a neural population. *Nature*, 440(7087):1007.

Schröder, C., Lagnado, L., James, B., and Berens, P. (2019). Approximate bayesian inference for a mechanistic model of vesicle release at a ribbon synapse. *BioRxiv*, page 669218.

Simonyan, K. and Zisserman, A. (2015). Very deep convolutional networks for large-scale image recognition. In *International Conference on Learning Representations*.

Sisson, S. A., Fan, Y., and Tanaka, M. M. (2007). Sequential monte carlo without likelihoods. *Proceedings of the National Academy of Sciences*, 104(6):1760–1765.

Speiser, A., Yan, J., Archer, E. W., Buesing, L., Turaga, S. C., and Macke, J. H. (2017). Fast amortized inference of neural activity from calcium imaging data with variational autoencoders. In *Advances in Neural Information Processing Systems*, pages 4024–4034.

Sporns, O. (2014). Contributions and challenges for network models in cognitive neuroscience. *Nature Neuroscience*, 17(5):652.

Stringer, C., Pachitariu, M., Steinmetz, N. A., Okun, M., Bartho, P., Harris, K. D., Sahani, M., and Lesica, N. A. (2016). Inhibitory control of correlated intrinsic variability in cortical networks. *eLife*, 5.

Suk, H.-J., Boyden, E. S., and van Welie, I. (2019). Advances in the automation of whole-cell patch clamp technology. *Journal of Neuroscience Methods*, 326:108357.

Sussillo, D. and Abbott, L. F. (2009). Generating coherent patterns of activity from chaotic neural networks. *Neuron*, 63(4):544–557.

Sussillo, D. and Barak, O. (2013). Opening the black box: low-dimensional dynamics in high-dimensional recurrent neural networks. *Neural Computation*, 25(3):626–649.

Talts, S., Betancourt, M., Simpson, D., Vehtari, A., and Gelman, A. (2018). Validating bayesian inference algorithms with simulation-based calibration. *arXiv preprint arXiv:1804.06788*.

Taylor, A. L., Goaillard, J.-M., and Marder, E. (2009). How multiple conductances determine electrophysiological properties in a multicompartment model. *Journal of Neuroscience*, 29(17):5573–5586.

Taylor, A. L., Hickey, T. J., Prinz, A. A., and Marder, E. (2006). Structure and visualization of high-dimensional conductance spaces. *Journal of Neurophysiology*, 96(2):891–905.

Teeter, C., Iyer, R., Menon, V., Gouwens, N., Feng, D., Berg, J., Szafer, A., Cain, N., Zeng, H., Hawrylycz, M., et al. (2018). Generalized leaky integrate-and-fire models classify multiple neuron types. *Nature Communications*, 9(1):709.

Tejero-Cantero, A., Boelts, J., Deistler, M., Lueckmann, J.-M., Durkan, C., Gonçalves, P. J., Greenberg, D. S., and Macke, J. H. (2020). sbi: A toolkit for simulation-based inference. *Journal of Open Source Software*, 5(52):2505.

Tomm, C., Avermann, M., Vogels, T., Gerstner, W., and Petersen, C. (2011). The influence of structure on the response properties of biologically plausible neural network models. *BMC neuroscience*, 12(1):P30.

Truccolo, W., Eden, U. T., Fellows, M. R., Donoghue, J. P., and Brown, E. N. (2005). A point process framework for relating neural spiking activity to spiking history, neural ensemble, and extrinsic covariate effects. *Journal of Neurophysiology*, 93(2):1074–1089.

Van Geit, W., Gevaert, M., Chindemi, G., Rössert, C., Courcol, J., Muller, E. B., Schürmann, F., Segev, I., and Markram, H. (2016). Bluepyopt: Leveraging open source software and cloud infrastructure to optimise model parameters in neuroscience. *Frontiers in Neuroinformatics*, 10:17.

van Vreeswijk, C. and Sompolinsky, H. (1996). Chaos in neuronal networks with balanced excitatory and inhibitory activity. *Science*, 274(5293).

Vogels, T. P., Rajan, K., and Abbott, L. F. (2005). Neural network dynamics. *Annual Review of Neuroscience*, 28:357–376.

Wang, X.-J. (2008). Decision making in recurrent neuronal circuits. *Neuron*, 60(2):215–234.

Webb, S., Golinski, A., Zinkov, R., Narayanaswamy, S., Rainforth, T., Teh, Y. W., and Wood, F. (2018). Faithful inversion of generative models for effective amortized inference. In *Advances in Neural Information Processing Systems*, pages 3070–3080.

Wilkinson, R. (2014). Accelerating abc methods using gaussian processes. In *AISTATS*.

Wood, S. N. (2010). Statistical inference for noisy nonlinear ecological dynamic systems. *Nature*, 466(7310).

Yu, B. M., Cunningham, J. P., Santhanam, G., Ryu, S. I., Shenoy, K. V., and Sahani, M. (2009). Gaussian-process factor analysis for low-dimensional single-trial analysis of neural population activity. *Journal of Neurophysiology*, 102(1):614–35.

Zitzler, E. and Künzli, S. (2004). Indicator-based selection in multiobjective search. In *International conference on parallel problem solving from nature*, pages 832–842. Springer.

Appendix 1

Supplementary figures

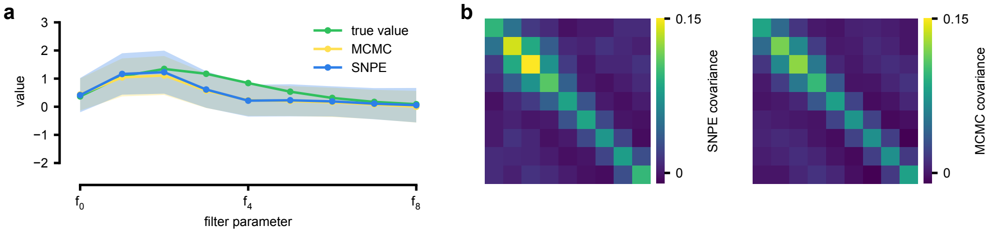

Appendix 1 Figure 1. Comparison between SNPE-estimated posterior and reference posterior (obtained via MCMC) on LN model. (a) Posterior mean ± one standard deviation of temporal filter (receptive field) from SNPE posterior (SNPE, blue) and reference posterior (MCMC, yellow). (b) Full covariance matrices from SNPE posterior (left) and reference (MCMC, right).

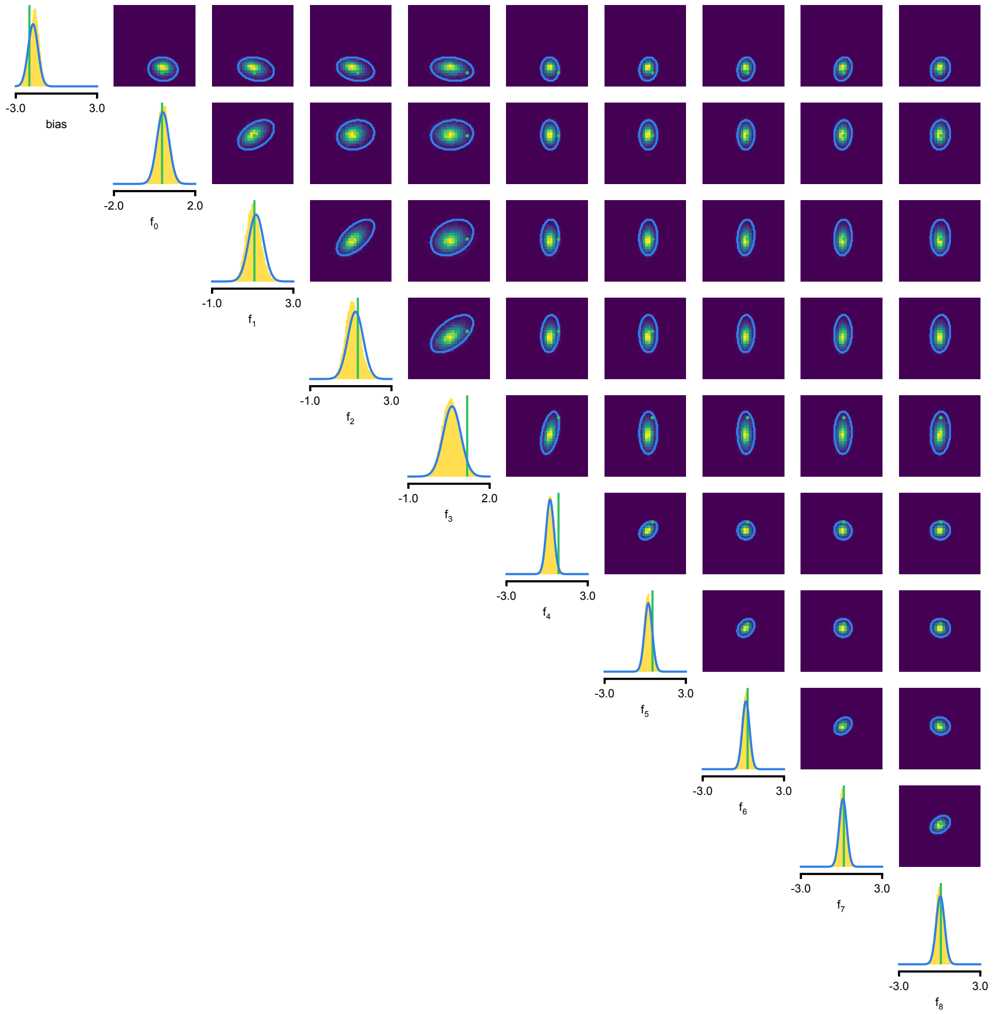

Appendix 1 Figure 2. Full posterior for LN model. In green, ground-truth parameters. Marginals (blue lines) and 2D marginals for SNPE (contour lines correspond to 95% of the mass) and MCMC (yellow histograms).

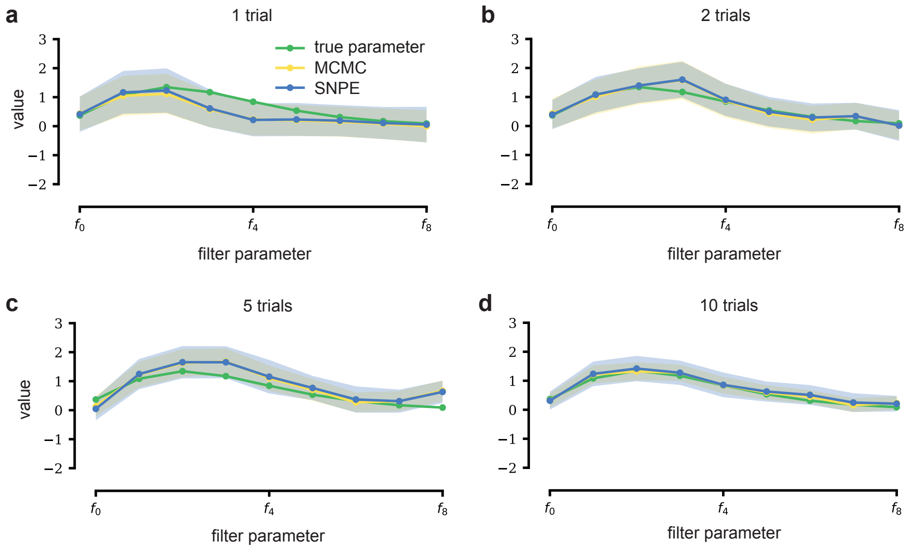

Appendix 1 Figure 3. LN model with additional data. With additional data, posterior samples cluster more tightly around the true filter. From left to right and top to bottom, SNPE (blue) and MCMC (yellow, for reference) are applied to observations with more independent Bernoulli trials, leading to progressively tighter posteriors and posterior samples closer to the true filter (which is the same across panels). Mean ± one standard deviation is shown. Note that SNPE closely agrees with the MCMC reference solution in all cases (a-d).

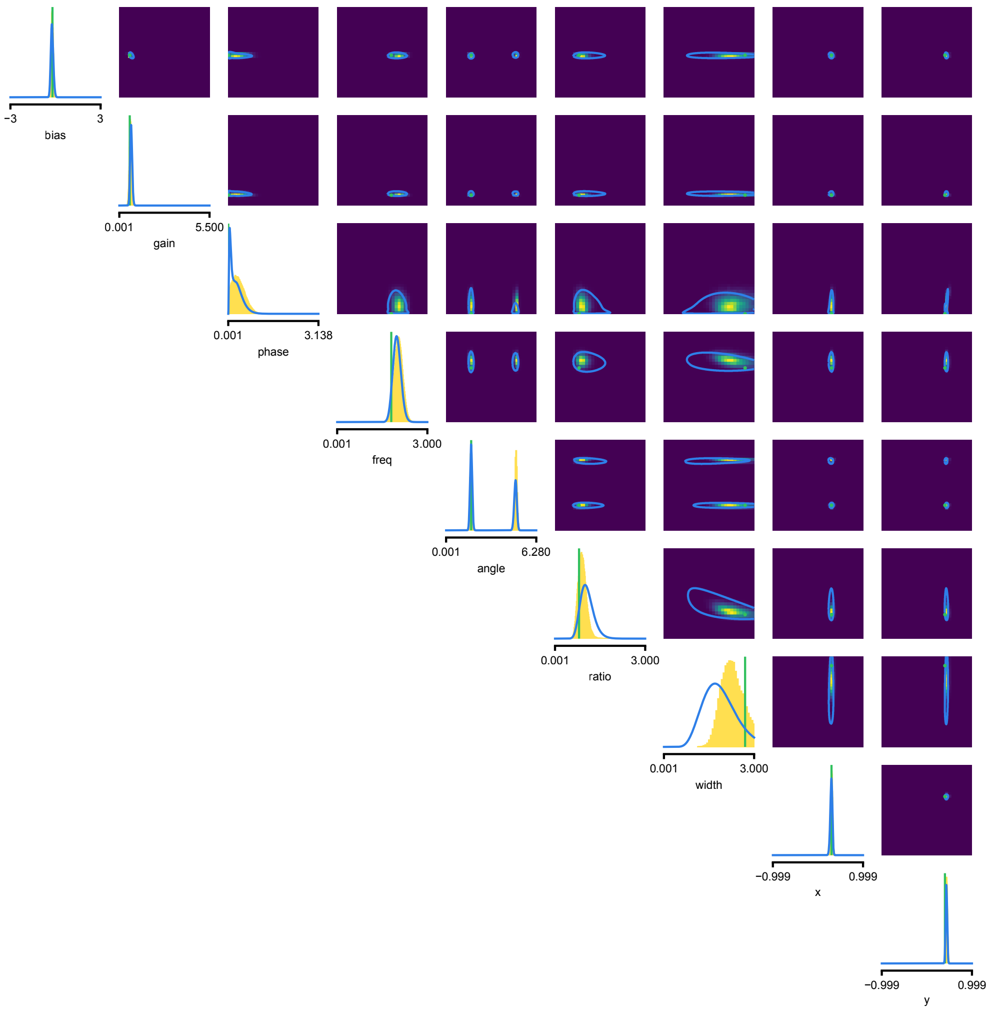

Appendix 1 Figure 4. Full posterior for Gabor GLM receptive field model. SNPE posterior estimate (blue lines) compared to reference posterior (MCMC, histograms). Ground-truth parameters used to simulate the data in green. We depict the distributions over the original receptive field parameters, whereas we estimate the posterior as a Gaussian mixture over transformed parameters, see Methods for details. We find that a (back-transformed) Gaussian mixture with four components approximates the posterior well in this case.

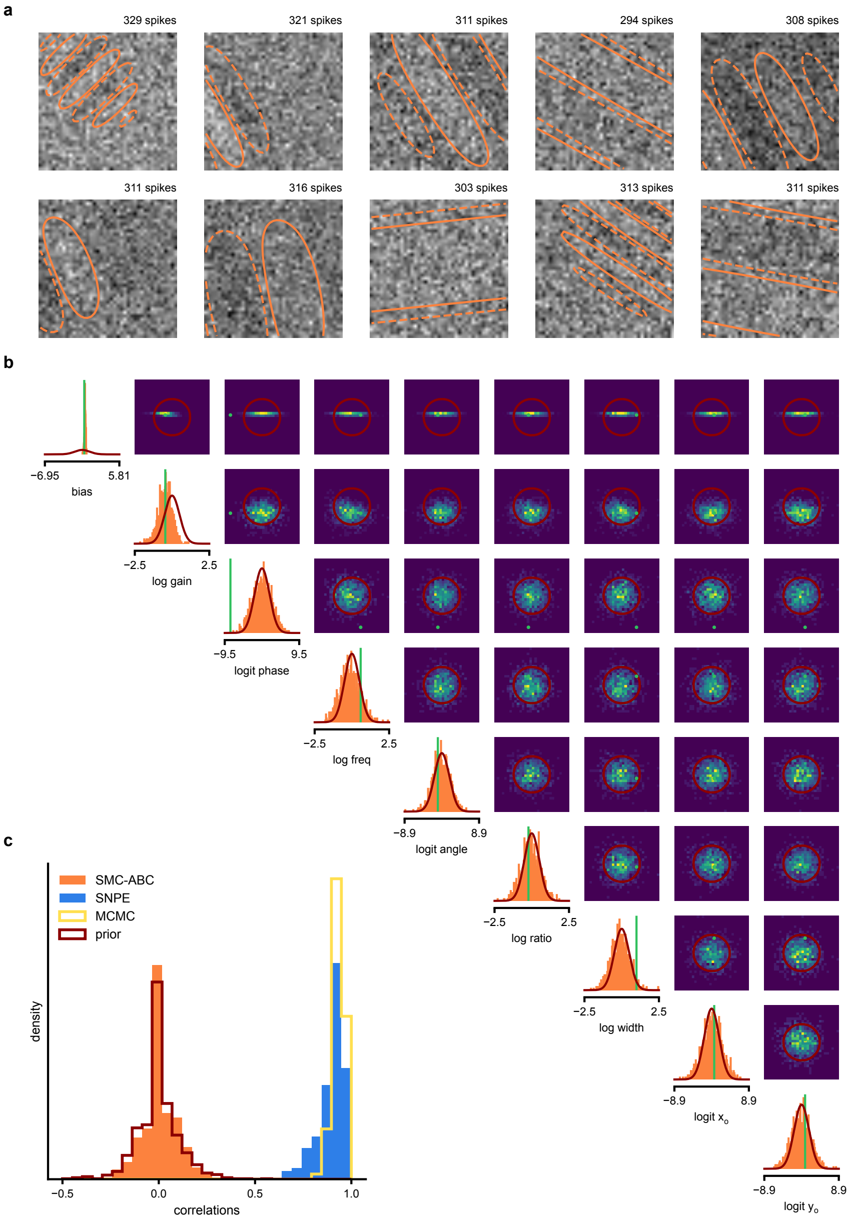

Appendix 1 Figure 5. SMC-ABC posterior estimate for Gabor GLM receptive field model. (a) Spike-triggered averages (STAs) and spike counts with closest distance $d(x_o, x_i)$ to the observed data x_o out of 10000 simulations with θ_i sampled from the prior. Spike counts are comparable to the observed data (x_o: 299 spikes), but receptive fields (contours) are not well constrained. (b) Results for SMC-ABC with 10^6 simulations total. Histograms of 1000 particles (orange) returned in the final iteration of SMC-ABC, compared to prior (red contour lines) and ground-truth parameters (green). Distributions over (log-/logit-)transformed parameters, axis limits scaled to mean ± 3 standard deviations of the prior. (c) Correlations between ground-truth receptive field and receptive fields sampled from SMC-ABC posterior (orange), SNPE posterior (blue), reference MCMC posterior (yellow) and prior (red). The SNPE-estimated receptive fields are almost as good as those of the reference posterior, the SMC-ABC estimated ones no better than the prior.

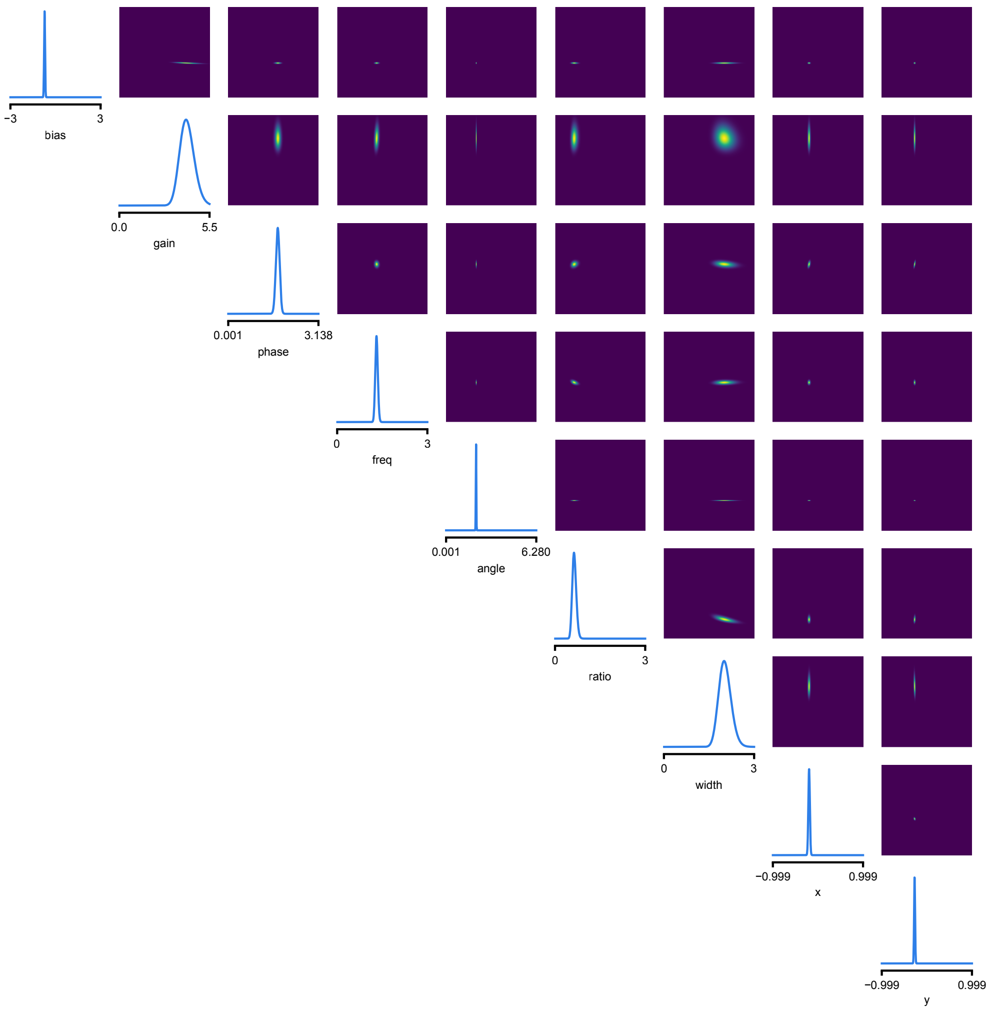

Appendix 1 Figure 6. Full posterior for Gabor LN receptive field model on V1 recordings. We depict the distributions over the receptive field parameters, derived from the Gaussian mixture over transformed-parameters (see Methods for details).

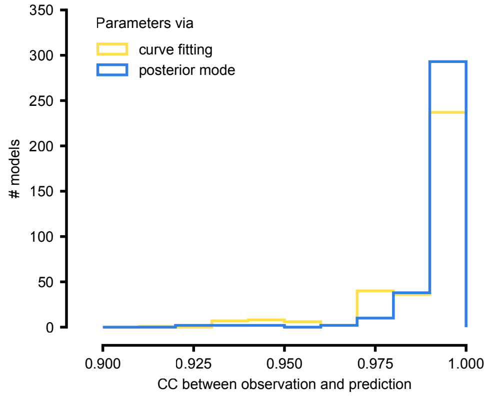

Appendix 1 Figure 7. Summary results on 350 ICG channel models, and comparison with direct fits. We generate predictions either with the posterior mode (blue) or with parameters obtained by directly fitting steady-state activation and time-constant curves (yellow). We calculate the correlation coefficient (CC) between observation and prediction. The distribution of CCs is similar for both approaches.

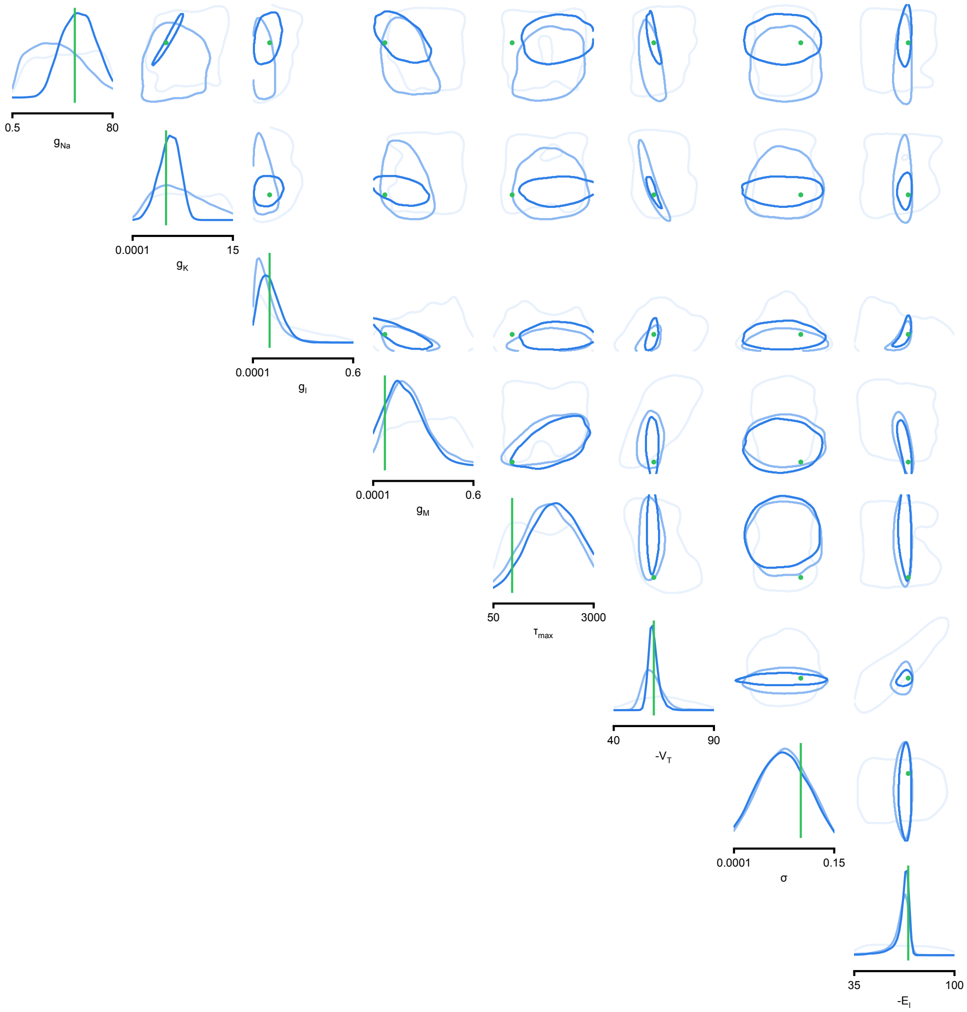

Appendix 1 Figure 8. Full posteriors for Hodgkin-Huxley model for 1, 4 and 7 features. Images show the pairwise marginals for 7 features. Each contour line corresponds to 68% density mass for a different inferred posterior. Light blue corresponds to 1 feature and dark blue to 7 features. Ground truth parameters in green.

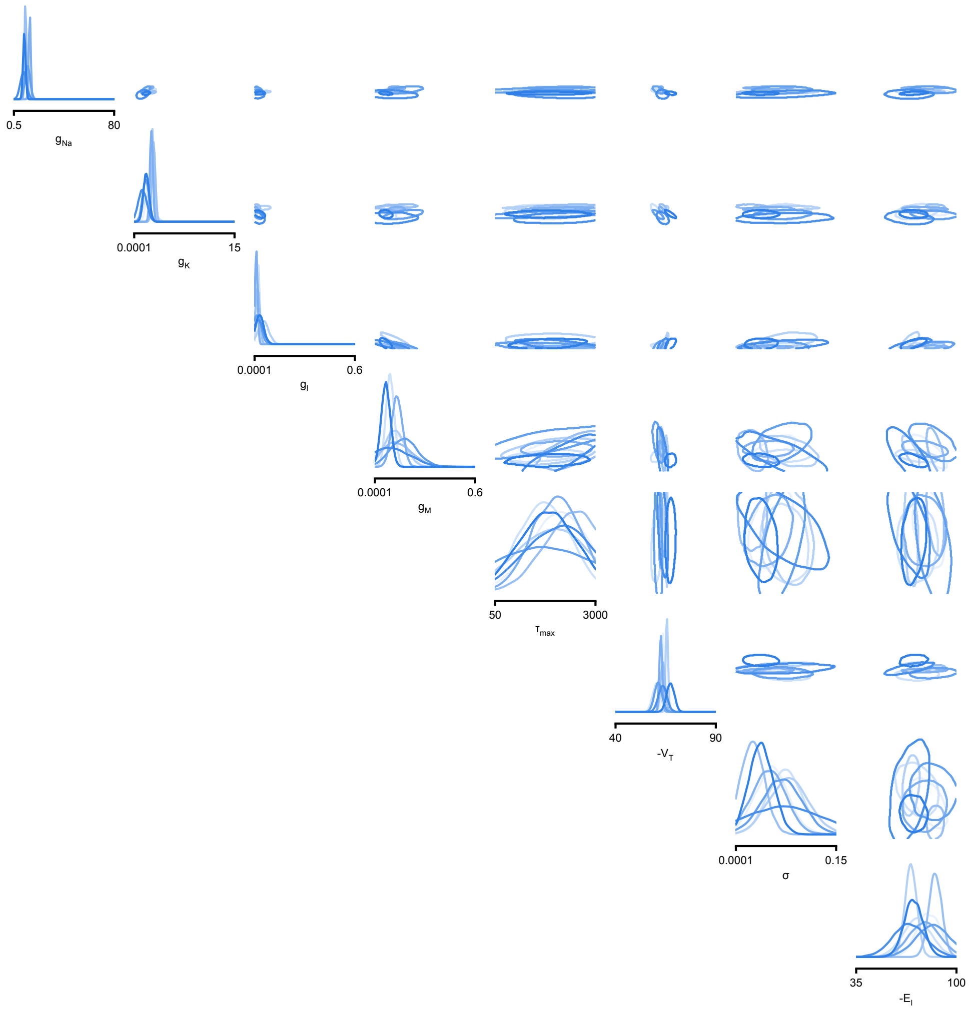

Appendix 1 Figure 9. Full posteriors for Hodgkin-Huxley model on 8 different recordings from Allen Cell Type Database. Images show the pairwise marginals for 7 features. Each contour line corresponds to 68% density mass for a different inferred posterior.

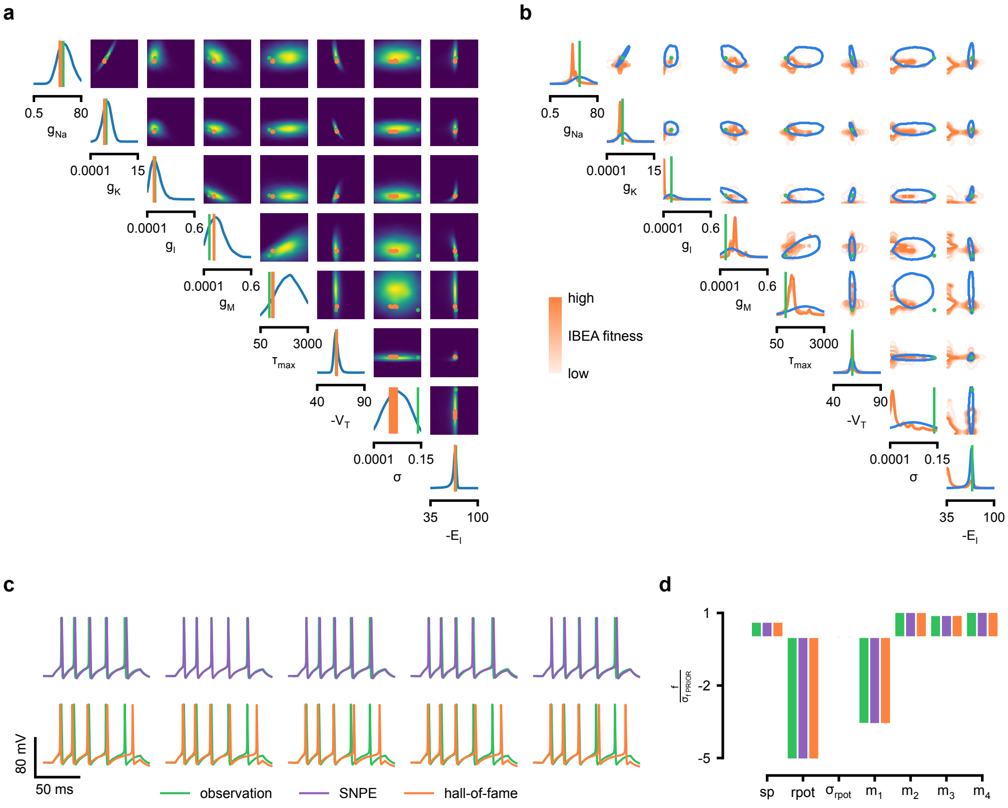

Appendix 1 Figure 10. Comparison between SNPE posterior and IBEA samples for Hodgkin-Huxley model with 8 parameters and 7 features. (a) Full SNPE posterior distribution. Ground truth parameters in green and IBEA 10 parameters with highest fitness ('hall-of-fame') in orange. (b) Blue contour line corresponds to 68% density mass for SNPE posterior. Light orange corresponds to IBEA sampled parameters with lowest IBEA fitness and dark orange to IBEA sampled parameters with highest IBEA fitness. This plot shows that, in general, SNPE and IBEA can return very different answers– this is not surprising, as both algorithms have different objectives, but this highlights that genetic algorithms do not in general perform statistical inference. (c) Traces for samples with high probability under SNPE posterior (purple), and for samples with high fitness under IBEA objective (hall-of-fame; orange traces). (d) Features for the desired output (observation), the mode of the inferred posterior (purple) and the best sample under IBEA objective (orange). Each voltage feature is normalized by $\sigma_{f\ \mathrm{PRIOR}}$, the standard deviation of the respective feature of simulations sampled from the prior.

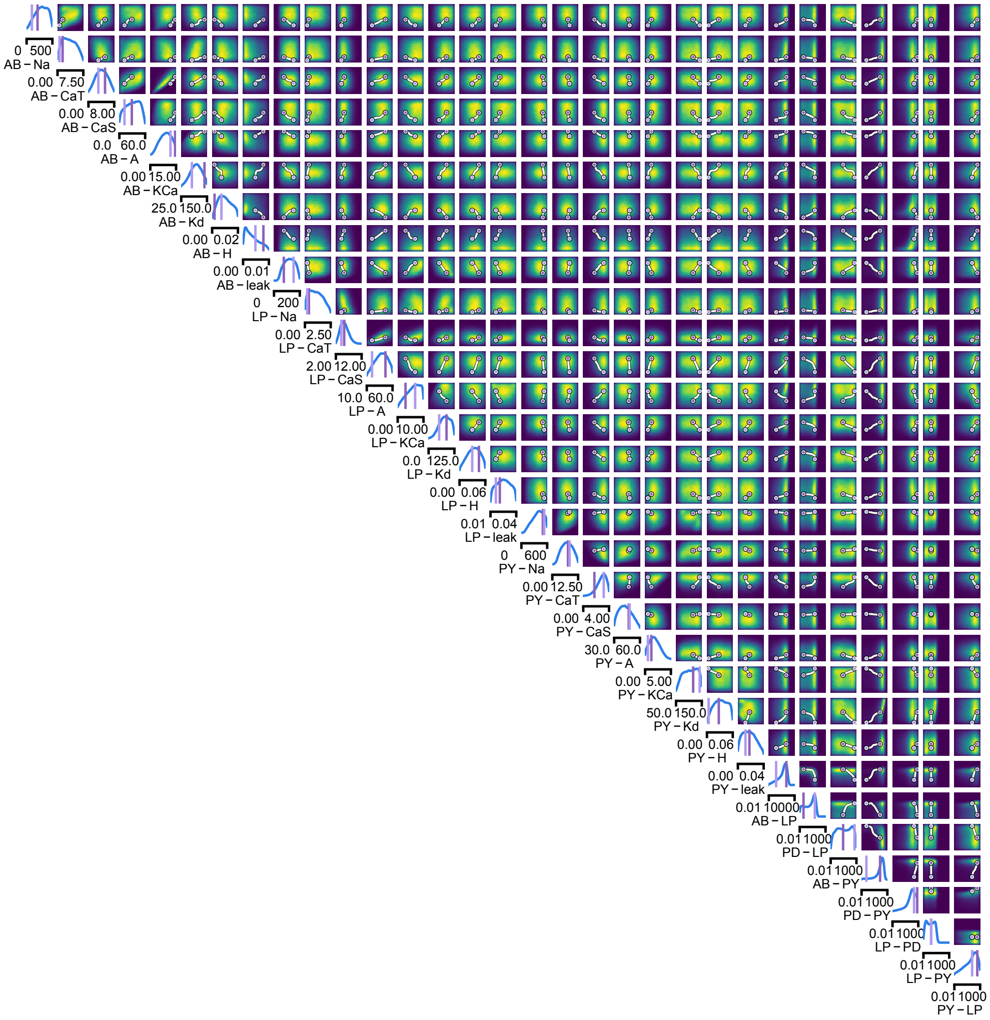

Appendix 1 Figure 11. Full posterior for the stomatogastric ganglion over 24 membrane and 7 synaptic conductances. The first 24 dimensions depict membrane conductances (top left), the last 7 depict synaptic conductances (bottom right). All synaptic conductances are logarithmically spaced. Between two samples from the posterior with high posterior probability (purple dots), there is a path of high posterior probability (white).

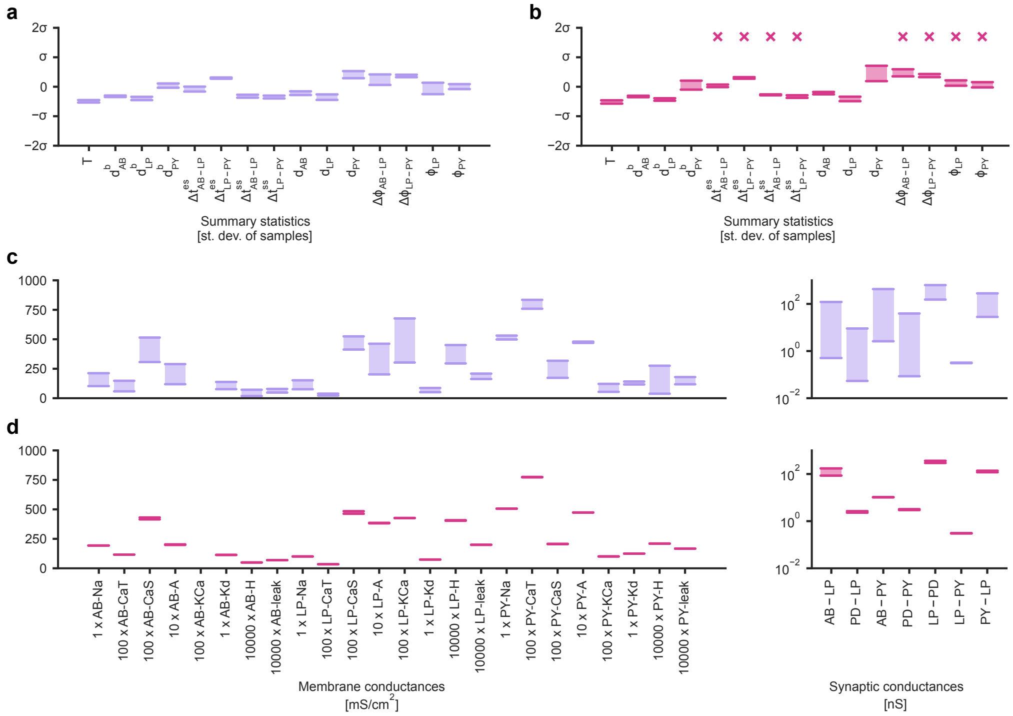

Appendix 1 Figure 12. Identifying directions of sloppiness and stiffness in the pyloric network of the crustacean stomatogastric ganglion. (a) Minimal and maximal values of all summary statistics along the path lying in regions of high posterior probability, sampled at 20 evenly spaced points. Summary statistics change only little. The summary statistics are z-scored with the mean and standard deviation of the 170,000 bursting samples in the created dataset. (b) Summary statistics sampled at 20 evenly spaced points along the orthogonal path. The summary statistics show stronger changes than in panel a and, in particular, often could not be defined because neurons bursted irregularly, as indicated by an 'x' above barplots. (c) Minimal and maximal values of the circuit parameters along the path lying in regions of high posterior probability. Both membrane conductances (left) and synaptic conductances (right) vary over large ranges. Axes as in panel (d). (d) Circuit parameters along the orthogonal path. The difference between the minimal and maximal value is much smaller than in panel (c).

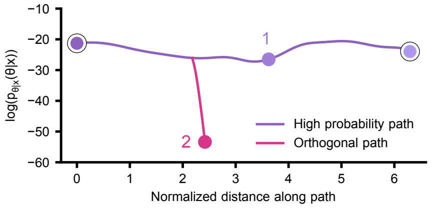

Appendix 1 Figure 13. Posterior probability along high probability and orthogonal path. Along the path that was optimized to lie in regions of high posterior probability (purple), the posterior probability remains relatively constant. Along the orthogonal path (pink), optimized to quickly reduce posterior probability, the probability quickly drops. The start and end points as well as the points labeled 1 and 2 correspond to the points shown in Fig. 5c.

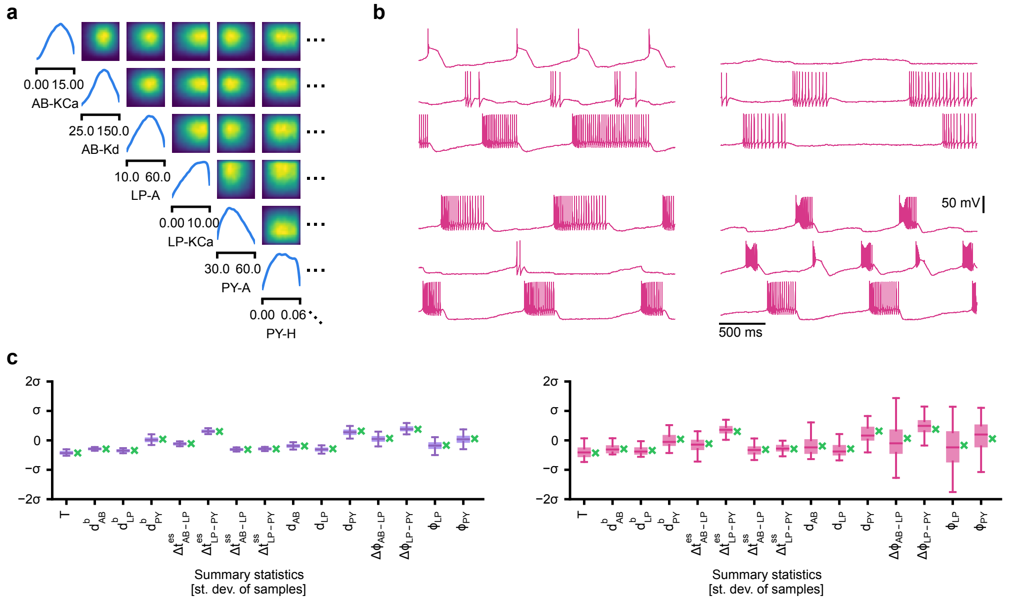

Appendix 1 Figure 14. Evaluating circuit configurations in which parameters have been sampled independently (a) Factorized posterior, i.e. posterior obtained by sampling each parameter independently from the associated marginals. Many of the pairwise marginals look similar to the full posterior shown in Supplementary Fig. 11, as the posterior correlations are low. (b) Samples from the factorized posterior– only a minority of these samples produce pyloric activity, highlighting the significance of the posterior correlations between parameters. (c) Left: summary features for 500 samples from the posterior. Boxplot for samples where all summary features are well-defined (80 % of all samples). Right: summary features for 500 samples from the factorized posterior. Only 23 % of these samples have well-defined summary features. The summary features from the factorized posterior have higher variation than the posterior ones. Summary features are z-scored using the mean and standard deviation of all samples in our training dataset obtained from prior samples. The boxplots indicate the maximum, 75% quantile, median, 25% quantile, and minimum. The green 'x' indicates the value of the experimental data (the observation, shown in Fig. 5b).